AGU PUBLICATIONS

Paleoceanography

RESEARCH ARTICLE
10.1002/2016PA002936

Key Points:
- Combined silicon isotope signatures and diatom assemblages trace productivity and upwelling intensity
- Latitudinal shifts of Peruvian upwelling center mainly responded to movements of the SWW and ITCZ
- Isotopic compositions of upwelled subsurface waters off Peru not significantly influenced by changes in preformed nutrients

Supporting Information:
- Tables S1–S4
- Supporting Information S1

Correspondence to:
K. Doering,
kdoering@geomar.de

Citation:
Doering, K., Z. Erdem, C. Ehlert, S. Fleury, M. Frank, and R. Schneider (2016), Changes in diatom productivity and upwelling intensity off Peru since the Last Glacial Maximum: Response to basin-scale atmospheric and oceanic forcing, *Paleoceanography*, *31*, 1453–1473, doi:10.1002/2016PA002936.

Received 18 FEB 2016
Accepted 3 OCT 2016
Accepted article online 6 OCT 2016
Published online 29 OCT 2016

Changes in diatom productivity and upwelling intensity off Peru since the Last Glacial Maximum: Response to basin-scale atmospheric and oceanic forcing

Kristin Doering[1], Zeynep Erdem[2], Claudia Ehlert[3], Sophie Fleury[4], Martin Frank[1], and Ralph Schneider[5]

[1]GEOMAR Helmholtz Centre for Ocean Research Kiel, Kiel, Germany, [2]Marine Microbiology and Biogeochemistry, Royal Netherlands Institute for Sea Research, Den Burg, Netherlands, [3]Max Planck Research Group for Marine Isotope Geochemistry, Institute for Chemistry and Biology of the Marine Environment (ICBM), University of of Oldenburg, Oldenburg, Germany, [4]Department of Marine Science and Convergence Technology, Hanyang University ERICA campus, Ansan, South Korea, [5]Institute of Geosciences, University of Kiel, Kiel, Germany

Abstract New records of stable silicon isotope signatures (δ^{30}Si) together with concentrations of biogenic opal and organic carbon from the central (9°S) and northern (5°S) Peruvian margin reveal changes in diatom productivity and nutrient utilization during the past 20,000 years. The findings are based on a new approach using the difference between the δ^{30}Si signatures of small (11–32 μm) and large (>150 μm) diatom fractions ($\Delta^{30}Si_{Coscino\text{-}bSi}$) in combination with the variance in diatom assemblages for reconstruction of past upwelling intensity. Combination of our records with two previously published records from the southern upwelling area off Peru (12–15°S) shows a general decoupling of the environmental conditions at the central and southern shelf mainly caused by a northward shift of the main upwelling cell from its modern position (12–15°S) toward 9°S during Termination 1. At this time only moderate upwelling intensity and productivity levels prevailed between 9°S and 12°S interpreted by a more northerly position of Southern Westerly Winds and the South Pacific Subtropical High. Furthermore, a marked decrease in productivity at 12–15°S during Heinrich Stadial 1 coincided with enhanced biogenic opal production in the Eastern Equatorial Pacific, which was induced by a southward shift of the Intertropical Convergence Zone and enhanced northeasterly trade winds. Modern conditions were only established at the onset of the Holocene. Past changes in preformed δ^{30}Si signatures of subsurface waters reaching the Peruvian Upwelling System did not significantly affect the preserved δ^{30}Si signatures.

1. Introduction

The Eastern Equatorial Pacific (EEP) hosts areas of pronounced biological productivity, the variability of which has been closely coupled with global climate and the carbon cycle [*Chavez and Barber*, 1987]. Modern and past variability of the system on seasonal and interannual timescales has been shown to be controlled by oceanic and atmospheric circulation, e.g., the meridional shifts of the Intertropical Convergence Zone (ITCZ), the Walker and Hadley circulation as well as El Niño–Southern Oscillation (ENSO) [*Barber and Chávez*, 1983; *Fiedler and Talley*, 2006; *Pennington et al*., 2006]. Superimposed on seasonal ocean-atmosphere cycles, interannual variability is generated by the ENSO [*Cane*, 2005], characterized by sea surface temperature (SST) anomalies affecting the seasonal shifts of the ITCZ [*Garreaud et al*., 2009]. However, there is conflicting evidence about the role of the ENSO-like variability on glacial-interglacial timescales. While some studies concluded the prevalence of an El Niño-like mean climate state during Termination 1 (T1; 19–11.7 ka B.P.), others favored hypothesis of a La Niña-like mean state [*Koutavas et al*., 2006; *Pena et al*., 2008; *Stott*, 2002].

Paleoceanographic studies of the EEP climate system have suggested that millennial to glacial-interglacial scale variations were triggered either by ocean-atmosphere interaction and orbital parameters controlling the position of the ITCZ or by changes in the intensity of the Atlantic Meridional Overturning Circulation (AMOC) causing stronger equatorial upwelling via the intensification of the northeastern (NE) trade winds [*Timmermann et al*., 2007; *Sifeddine et al*., 2008; *Gutiérrez et al*., 2009; *Kienast et al*., 2013; *Dubois et al*., 2014; *Salvatteci et al*., 2014b]. For instance, reconstructions of sea surface and subsurface temperatures (SST) from the equatorial Pacific have been applied to estimate the Walker circulation strength [*Kienast et al*., 2013] and foraminifera-based stable isotope records (δ^{18}O and δ^{13}C) [*Spero*, 2002; *Pena et al*., 2008] to evaluate changes

in subsurface water supply via "ocean tunneling" between the Southern Ocean and low latitudes since the Last Glacial Maximum (LGM; 23–19 ka B.P.). These studies have suggested that during Heinrich Stadial 1 (HS1; 18–15 ka B.P.) the ITCZ moved southward (i.e., El Niño-like mean state) in response to Northern Hemisphere cooling and to AMOC reduction that caused enhanced equatorial upwelling by the intensification of the Central American gap wind system (e.g., NE trade winds) [*Timmermann et al*., 2007; *Kienast et al*., 2013; *Dubois et al*., 2014]. In contrast, equatorial eolian dust analyses [*Xie and Marcantonio*, 2012; *bin Shaari et al*., 2013] indicated a northward shift of the ITCZ during Termination 1 (19 ka to 11 ka B.P.; T1). This is supported by a saltier thermocline ($\delta^{18}O$, $\delta^{13}C$, and Mg/Ca measurements) [*Pena et al*. [2008]) and increased diatom productivity (biomarkers) [*Makou et al*. [2010]) reflecting a La Niña-like mean state.

The changes described above should be directly reflected in marked variations in past upwelling intensity, diatom productivity, and thus nutrient utilization off Peru, but there are not many detailed records available [*De Vries and Schrader*, 1981; *Schrader and Sorknes*, 1991; *Schrader*, 1992]. Today, the high nutrient availability in the coastal area off Peru promotes a phytoplankton community that is dominated by diatoms [*Blasco*, 1971; *Estrada and Blasco*, 1985; *Bruland et al*., 2005; *DiTullio et al*., 2005]. High export rates of biogenic opal via episodic diatom bloom events are recorded in laminated sediments of the essentially oxygen-free bottom waters beneath the upwelling centers on the Peruvian shelf [*Brodie and Kemp*, 1994; *Salvatteci et al*., 2014a; *Fleury et al*., 2015; *Schönfeld et al*., 2015].

Variations in past productivity as well as changes in the diatom community have been shown to indicate shifts between the proposed El Niño- and La Niña-like mean states that reflect larger-scale oceanographic and climatic changes [*Fleury et al*., 2015]. At multicentennial scale, Northern Hemisphere cold periods (e.g., the Little Ice Age (LIA); 1400–1850 A.D.), the Peruvian Upwelling Ecosystem (PUE) was characterized by strongly diminished biological productivity and nutrient utilization associated with a deeper thermocline, i.e., an El Niño-like mean state. This was paralleled by a weakened Walker circulation and associated trade winds [*Sifeddine et al*., 2008; *Gutiérrez et al*., 2009; *Ehlert et al*., 2015] as well as by higher precipitation caused by a southward shift of the ITCZ [*Gutiérrez et al*., 2009; *Sachs et al*., 2009]. In contrast, during warm periods (e.g., the Medieval Climate Anomaly; 900–1350 A.D.) productivity markedly increased, mainly caused by enhanced Walker circulation, more intense trade winds, and a shallower thermocline in conjunction with a northerly position of the ITCZ and a strengthened South Pacific Subtropical High (SPSH) [*Gutiérrez et al*., 2009; *Salvatteci et al*., 2014b; *Ehlert et al*., 2015]. However, it remained always difficult to unravel whether climate change at such timescales had similar or different effects on upwelling intensity, productivity, and nutrient utilization, preventing full understanding of the complex interplay between forcing and response mechanisms in the PUE.

In recent years the application of stable silicon isotope ($\delta^{30}Si$) compositions of sedimentary diatoms has been successfully established as an indicator for past dissolved silicic acid ($Si(OH)_4$) utilization by diatoms in surface waters. Several studies investigated the modern [*Beucher et al*., 2008, 2011; *Ehlert et al*., 2012; *Grasse et al*., 2013] and past silicon (Si) cycle in the EEP [*Pichevin et al*., 2009] and PUE [*Ehlert et al*., 2013]. These studies showed that intense upwelling and productivity are associated with stronger utilization of surface water Si $(OH)_4$ by diatoms in upwelling regions, which leads to overall high $\delta^{30}Si$ signatures of diatom frustules preserved in the underlying sediments [*Pichevin et al*., 2014; *Ehlert et al*., 2013, 2015]. Furthermore, the differentiation between $\delta^{30}Si$ signatures of small diatom species and large handpicked diatom species recently supported their linkage to upwelling intensity [*Doering et al*., 2016]. This approach is based on the finding that the larger diatom species reflect stratified conditions and near-complete nutrient utilization indicated by high $\delta^{30}Si_{Coscino}$ values. In contrast, the $\delta^{30}Si_{bSi}$ signatures of small diatom species record the gradual increase in seawater $\delta^{30}Si$ as a result of progressive $Si(OH)_4$ utilization during intense bloom events in direct response to the strength of upwelling [*Doering et al*., 2016]. Hence, variable degrees of upwelling intensity and silicate utilization along the modern shelf result in lower $\delta^{30}Si_{bSi}$ signatures when upwelling was weak and vice versa, whereas $\delta^{30}Si_{Coscino}$ signatures show continuously high values reflecting the prevailing $Si(OH)_4$ limitation along the shelf during stratified conditions. Accordingly, $\Delta^{30}Si$ values are lowest in areas of most intense upwelling conditions and highest where weak upwelling and low $Si(OH)_4$ concentrations do not permit intense blooms [*Doering et al*., 2016]. However, a substantial influence of the diatom assemblage on past $\delta^{30}Si$ records due to species-specific fractionation factors, as reported previously [*Sutton et al*., 2013], could be excluded by the applicable estimations off Peru so far [*Doering et al*., 2016].

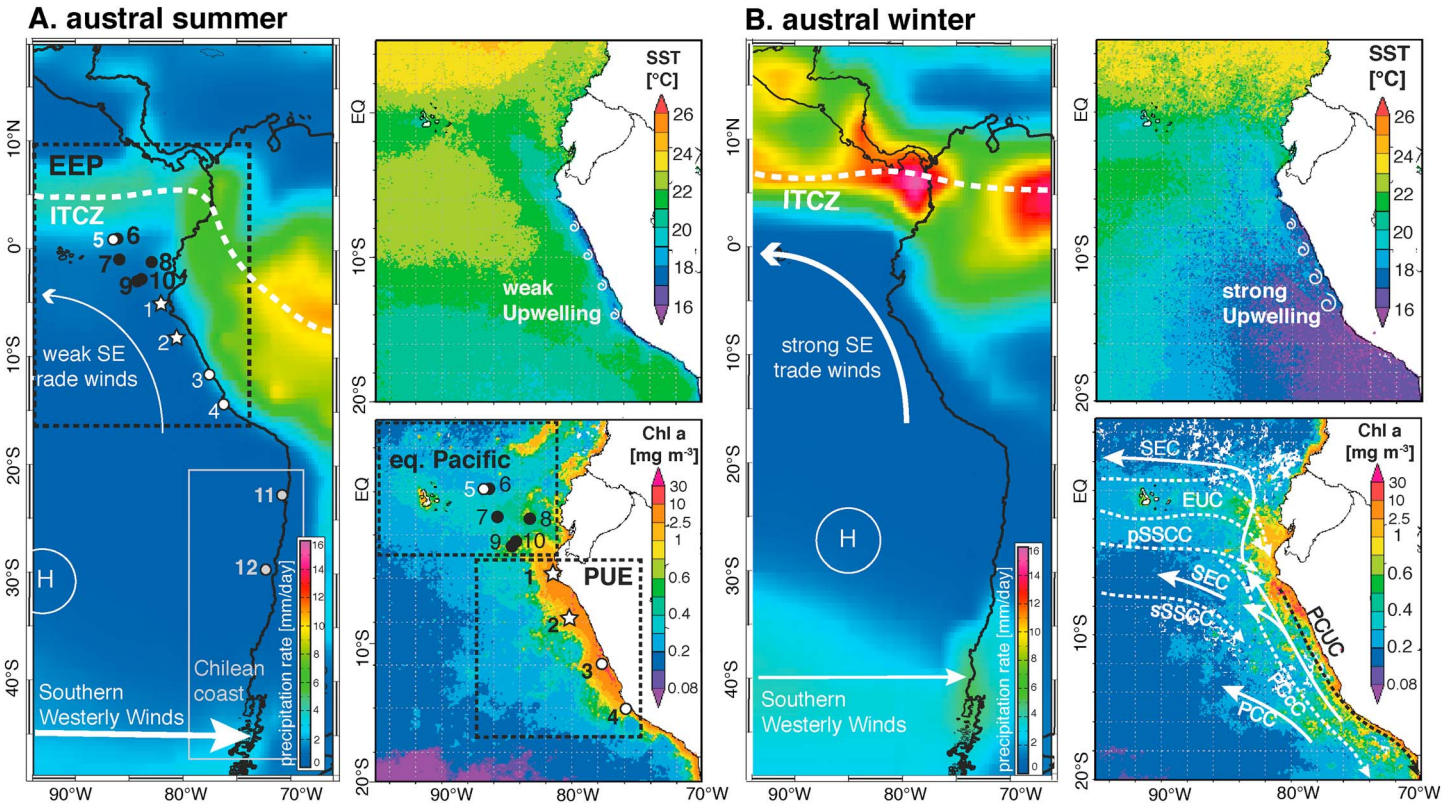

Figure 1. Comparison of environmental parameters controlling present-day austral summer and winter conditions off Peru: (a) austral summer; Left: Mean precipitation rate (mm/day; June–August). The position of the ITCZ is indicated by white dotted lines, and the approximate position of the Subtropical High is marked (H). The black (EEP) and gray (Chilean coast) circles indicate core sites used for comparison of opal fluxes, white circles indicate cores sites used for comparison of stable silicon isotope records, while white stars indicate the two new cores presented in this study (see Table 2). Right top: Mean Sea Surface Temperatures (SST). Right bottom: Chlorophyll *a* concentration. (b) Austral winter; Left: Mean precipitation rate (mm/day; December–February); Right top: Mean Sea Surface Temperatures (SST); Right bottom: Chlorophyll *a* concentration; Solid white arrows indicate surface currents: SEC, South Equatorial Current; PCC, Peru-Chile-Current; PCCC, Peru Coastal Current. Dashed arrows show subsurface currents: EUC, Equatorial Undercurrent; pSSCC, primary Southern Subsurface Counter Current; sSSCC, secondary Subsurface Counter current; PCCC, Peru-Chile Counter Current; PCUC, Peru-Chile Undercurrent. Precipitation rates were averaged over the last 30 years (1980–2010) from NASA GPCP (http://iridl.ldeo.columbia.edu) [*Adler et al.*, 2003; *Huffman et al.*, 2009]. SST and Chl *a* are given for 2008 and were generated via http://oceancolor.gsfc.nasa.gov/cgi/. A list of the detailed locations and water depths of the cores displayed in Figure 1a is given in Table 1.

In this study we aim to resolve the regional response of the PUE to basin-scale atmospheric and oceanographic variability during the last transition from a glacial into an interglacial climate state. We combine the reconstruction of past productivity with those of nutrient utilization and upwelling intensity. Past productivity is derived from accumulation rates of biogenic opal (bSi) and particulate organic carbon (C_{org}), whereas nutrient utilization is reconstructed from the $\delta^{30}Si$ signatures of different diatom fractions (11–32 μm mixed diatom species: $\delta^{30}Si_{bSi}$ and >150 μm handpicked monogeneric diatoms *Coscinodiscus* spp.: $\delta^{30}Si_{Coscino}$). Upwelling intensity is determined based on a new approach using the difference ($\Delta^{30}Si$) between $\delta^{30}Si_{Coscino}$ and $\delta^{30}Si_{bSi}$ signatures ($\delta^{30}Si_{Coscino} - {}^{30}Si_{bSi}$) measured on the same sediment samples, as well as the diatom assemblage within the small diatom fraction (11–32 μm) [*Ehlert et al.*, 2012; *Doering et al.*, 2016].

2. Regional Setting

The climatic and oceanographic conditions in the EEP are a result of interactions of basin-scale atmospheric circulation with local effects occurring at the land sea interface [*Strub et al.*, 1998]. The SPSH drives equatorward winds along the western coast of South America (Figure 1). During austral winter, strong cross-equatorial southeast (SE) trade winds drive enhanced upwelling along northern South America causing surface cooling and an enhanced cross-equatorial SST gradient (Figure 1b) [*Wyrtki*, 1981]. During austral summer trade winds and upwelling weaken, which results in higher SSTs in the EEP and thus in a weaker

Table 1. Downcore Records of $\delta^{30}Si_{bSi}$, $\delta^{30}Si_{Coscino}$, and bSi of Cores M77/2-052, M77/2-029, and SO147-106KL[a]

M772-052						M772-029						SO147-106KL		
Age (ka B.P.)	bSi (wt %)	$\delta^{30}Si_{bSi}$ (‰)	2σ	$\delta^{30}Si_{Coscino}$ (‰)	2σ	Age (ka B.P.)	bSi (wt %)	$\delta^{30}Si_{bSi}$ (‰)	2σ	$\delta^{30}Si_{Coscino}$ (‰)	2σ	Age (ka B.P.)	$\delta^{30}Si_{Coscino}$ (‰)	2σ
0.37	10.29	1.06	0.20	1.39	0.26	2.94	3.23	0.28	0.09	-	-	1.17	1.38	0.11
1.11	6.80	1.58	0.13	1.48	0.18	4.71	5.92	0.10	0.22	1.00	0.25	1.34	*1.41*	*0.13*
1.86	7.87	1.60	0.21	1.60	0.12	8.13	4.61	0.15	0.25	0.78	0.24	1.39	*1.37*	*0.14*
3.34	7.61	0.96	0.17	-	-	9.51	6.43	0.36	0.18	0.96	0.18	1.56	0.89	0.17
5.20	6.38	-	-	1.43	0.19	10.63	8.28	0.11	0.16	0.96	0.11	1.86	*1.51*	*0.18*
5.57	7.77	1.42	0.25	-	-	11.51	12.74	0.81	0.09	0.94	0.18	2.45	*1.47*	*0.16*
7.06	5.62	0.95	0.25	-	-	12.64	17.84	0.13	0.24	1.31	0.14	3.13	0.83	0.10
10.77	5.57	1.20	0.11	-	-	12.99	26.32	0.87	0.13	-	-	3.42	0.51	0.13
11.51	4.25	1.25	0.22	-	-	13.26	16.93	0.45	0.32	-	-	3.80	0.62	0.07
11.88	4.30	-	-	0.84	0.17	13.67	17.94	0.77	0.13	-	-	5.94	0.42	0.22
12.63	6.44	-	-	1.32	0.12	14.00	15.43	1.08	0.15	-	-	8.93	1.15	0.21
13.00	6.78	1.67	0.16	-	-	14.15	22.83	1.19	0.23	1.53	0.19	9.11	*1.5*	*0.27*
13.74	4.19	0.65	0.21	1.61	0.14	14.32	19.04	1.25	0.12	-	-	9.26	1.22	0.16
14.71	4.35	-	-	1.65	0.11	15.04	32.12	1.25	0.25	-	-	10.21	1.30	0.08
15.68	5.69	1.82	0.19	-	-	15.16	20.44	1.07	0.28	-	-	10.32	*1.4*	*0.19*
16.65	5.67	-	-	1.48	0.15	15.57	-	1.27	0.16	1.43	0.11	12.02	1.30	0.08
18.59	9.30	1.41	0.23	-	-	15.71	23.79	0.99	0.15	-	-	13.26	*1.51*	*0.15*
19.07	5.63	-	-	1.65	0.32	15.79	-	1.35	0.15	-	-	13.79	0.83	0.09
						15.97	27.03	0.91	0.18	-	-	14.16	0.58	0.16
						16.10	36.24	1.02	0.13	-	-	16.03	0.98	0.19
						16.15	37.09	1.15	0.17	-	-			
						16.33	20.61	1.18	0.12	-	-			
						16.37	39.29	0.90	0.24	-	-			
						16.47	14.51	1.10	0.15	1.31	0.13			
						16.77	-	1.28	0.15	-	-			
						16.84	26.73	1.20	0.16	-	-			
						16.96	42.55	1.11	0.13	-	-			
						17.16	21.23	1.04	0.14	-	-			
						17.25	15.15	1.18	0.23	-	-			
						17.40	34.20	1.08	0.11	-	-			
						17.46	15.61	1.24	0.18	1.40	0.09			
						17.57	27.31	1.08	0.25	-	-			
						17.74	21.55	1.11	0.31	-	-			
						18.03	18.14	1.25	0.24	-	-			
						18.09	25.30	1.26	0.12	1.47	0.33			
						18.15	25.82	1.02	0.21	-	-			
						18.27	-	1.13	0.19	-	-			

[a]The 2σ error given for both $\delta^{30}Si_{bSi}$ and $\delta^{30}Si_{Coscino}$ indicates reproducibility based on replicate measurements. The bSi (wt %) data of core 029 were taken from *Mollier-Vogel* [2012]. The data of core SO147-106KL were taken from *Ehlert et al.* [2013], and new measurements of $\delta^{30}Si_{Coscino}$ for this core are marked in italic.

cross-equatorial SST gradient (Figure 1a) [*Chelton et al.*, 2001]. To the north the system is bordered by the ITCZ, which constitutes the belt of converging northern and southern trade winds, associated with intense convection and precipitation. Today, the ITCZ migrates between 3°N in austral summer (February–March; Figure 1a) and 10°N in austral winter (August–September; Figure 1b), respectively [*Wyrtki*, 1975; *Kessler*, 2006].

Along the Peruvian margin between 1°N and 18°S (Figure 1a) SE trade winds drive surface waters northward, thereby generating along the shore the Peru-Chile Coastal Current (PCCC) and farther offshore the Peru-Chile Current (PCC) (Figure 1b) [*Fiedler and Talley*, 2006, and references therein]. The southward flowing subsurface Peru-Chile Undercurrent (PCUC) is the main source of the waters upwelling off Peru [*Zuta and Guillén*, 1970; *Brink et al.*, 1983; *Toggweiler et al.*, 1991]. Approximately 30% of the PCUC waters originate from three subsurface currents [*Montes et al.*, 2010]: the eastward flowing subsurface waters of the Equatorial Undercurrent (EUC; 1.5°N–1.5°S), the primary Southern Subsurface Counter Current (pSSCC; 2°S–4.7°S), and the secondary Southern Subsurface Counter Current (sSSCC; 5.8–8.2°S) (Figure 1c) [*Brink et al.*, 1983; *Toggweiler et al.*, 1991]. The remaining 70% of the PCUC waters originate from upwelling from below the PCUC (35%) and

weak diffuse currents in the domain south of 9°S (35%) [*Montes et al*., 2010]. The PCUC reaches its maximum velocity between 6°S and 10°S, leading to decreased deposition of sediments and reworking of bottom sediments [*Suess et al*., 1987]. Farther south, the velocity of the subsurface current decreases allowing enhanced sediment deposition and high sedimentation rates along the upper continental slope [*Krissek et al*., 1980; *Suess et al*., 1987]. The shape of the coastline leads to the development of several main upwelling centers located today at 4–6°S, 7–9°S, 11–13°S, and 14–16°S [*Zuta and Guillén*, 1970; *de Mendiola*, 1981]. Although effects of erosion and reworking are often excluded because of the presence of finely laminated sediment intervals, modern sediments between 5°S and 10°S as well as sediment cores covering T1 and the Holocene reveal large discontinuities in the sediment record [*Skillbeck and Fink*, 2006; *Erdem et al*., 2016]. These discontinuities in the sedimentary record have been attributed to the erosion by strong bottom currents (velocity of the PCUC) [e.g., *Reimers and Suess*, 1983; *Reinhardt et al*., 2002; *Skillbeck and Fink*, 2006], earthquakes [*Salvatteci et al*., 2014a], and/or nonlinear internal waves (NLIWs) [see *Erdem et al*., 2016] causing sediment erosion and sediment redistribution or bioturbation caused by periodic bottom water oxygenation [*Levin*, 2003]. Nonetheless, recent reconstructions applying stacked sediment approaches have shown to produce reliable records focusing on laminated sediment sections [*Salvatteci et al*., 2014a].

Primary productivity (PP) off Peru is mainly controlled by the supply of macronutrients and micronutrients (e.g., nitrate, $Si(OH)_4$, phosphate, iron (Fe), and cadmium) [see *Messié and Chavez*, 2015]. The phytoplankton community is generally composed of early successional stages dominated by small diatoms (5–30 μm) with high reproduction rates, while later successional stages are characterized by larger-sized species [*MacIsaac et al*., 1985; *Tarazona et al*., 2003; *Doering et al*., 2016]. This change in specific composition is closely related to the transition from vertically mixed to more stratified conditions. In oceanic waters, which can be found farther offshore, the phytoplankton community is dominated by dinoflagellates and large diatoms with low reproduction and assimilation rates [*Ochoa and Gomez*, 1981; *Sanchez et al*., 2000; *Ochoa et al*., 2010].

El Niño events are characterized by warmer SSTs, the weakening of the trade winds, and a deepening of the thermocline in the eastern and central tropical Pacific. Consequently, during El Niño events upwelling delivers only warm, nutrient-poor waters to the surface due to a deepened thermocline [*Huyer et al*., 1987]. Tropical surface waters reach the Peruvian coast [*Sanchez et al*., 2000] reducing PP by about 50% and shifting the phytoplankton community to dinoflagellates and large subtropical diatom species [*Barber and Chávez*, 1983; *Chavez*, 1989]. In contrast, La Niña events are associated with a stronger Walker (west-east or zonal) circulation and a thermocline shoaling resulting in an intensification of the coastal cold tongue.

3. Material and Methods

This study presents new records of two piston cores together with two previously published records, which for the first time enable a reconstruction of upwelling intensity and utilization due to biogeochemical and oceanographic changes of the past 20,000 years along the entire Peruvian Margin (Figure 1). New records of $\delta^{30}Si$ signatures of both, small-mixed diatoms (11–32 μm; $\delta^{30}Si_{bSi}$) and larger handpicked diatoms (125/150–200 μm *Coscinodiscus* spp.; $\delta^{30}Si_{Coscino}$), accumulation rates of bSi ($g\,cm^{-2}\,ka^{-1}$), as well as diatom assemblage counts were generated for cores M77/2-029-3 (029; 9°17′S, 79°37′W, 444 m water depth) and M772-052-2 (052; 5°29′S, 81°27′W, 1249 m water depth). Both were retrieved during the German R/V *Meteor* cruise M77/2 in 2008, within the framework of the Collaborative Research Centre 754 (Sonderforschungsbereich/SFB 754). These new records are interpreted together with previously published records of cores M77/2-003-2 (003; 15°06′S, 75°41′W, 271 m water depth) [*Doering et al*., 2016] and SO147-106KL (106KL; 12°03′S, 77°40′W, 184 m water depth) [*Ehlert et al*., 2013], the latter of which was extended for this study by seven new $\delta^{30}Si_{Coscino}$ measurements for this study.

3.1. Core Descriptions

The sediment cores retrieved from the shelf (i.e., 029, 106KL, and 003) show the characteristic laminations consisting of alternating diatom ooze and dark olive gray sediment dominating large sections of the cores (Figure 2). Only sediment core 052, located considerably offshore at the northern rim of the PUE, consists of homogenous olive gray, foraminifera-bearing mud without any lamination. Likewise, the first 2 m of core 029 consists of a similar homogenous dark olive gray clayey/silty mud-bearing foraminifera, while the rest of the core (2–13.5 m) is characterized by finely laminated diatom ooze intercalated by olive and yellow silty clay

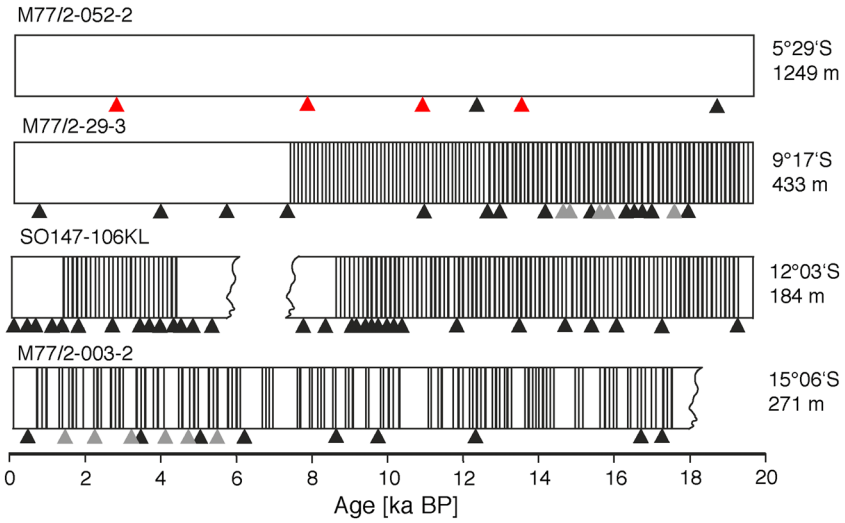

Figure 2. Distribution of laminated intervals in sediment cores 29, 106KL, and 003. Triangles depict radiocarbon ages (black: previously published) [see *Schönfeld et al*., 2015] (red: dating points of core M77/2-059 used for tuning; gray: new dating points presented in this study). Modified after *Schönfeld et al*. [2015].

(Figure 2). Similarly, sediment cores 106KL and 003 consist entirely of dark olive gray mud, intercalated with dark grayish to pale yellow laminated intervals of diatom ooze. Core 106KL is marked by a hiatus in the sedimentation at about 3 m depth (between 6 ka and 8 ka B.P.). Otherwise laminated sediments are found throughout the entire core rarely intermitted by short homogenous sections. In comparison, laminations in core 003 are more frequently interrupted by small slumps and indications of short intervals of bioturbation, but the sediment record otherwise continuously covers the past 17,700 years without major disturbances or hiatuses [*Doering et al*., 2016].

3.2. Age Models

The age model of core 052 [*Erdem et al*., 2016] is based on five Accelerator Mass Spectrometer (AMS) ^{14}C datings of the planktonic foraminifera species *Neogloboquadrina dutertrei* in combination with orbital tuning of $\delta^{18}O$ values of nearby core M77/2-059 [*Mollier-Vogel et al*., 2013] and supported by correlation to the $\delta^{18}O$ of the EPICA ice core [*European Project for Ice Coring in Antarctica Community Members*, 2006]. The conventional radiocarbon dates were calibrated using the software Calib 7.0 and applying the marine calibration set Marine13 [*Reimer and Bard*, 2013]. The age model of core 029 originally based on 11 AMS ^{14}C datings [*Mollier-Vogel*, 2012] was improved by six additional AMS ^{14}C measurements (see supporting information S1 and Table S1). All measurements were performed at the Leibniz Laboratory for Radiometric Dating Isotope Research and Dating at Kiel University. All ^{14}C ages were corrected by applying a reservoir age of 511 ± 278 years following *Ortlieb et al*. [2011]. The resulting ages were converted into calendar years using the program CLAM2.2 [*Blaauw*, 2010] and the Marine13 calibration curve (see supporting information Table S2) [*Reimer and Bard*, 2013]. CLAM2.2 was further used to provide a best fit between radiocarbon ages using a "smooth spline" age model (supporting information Figure S1). Published age models based on AMS ^{14}C ages were used for core 106KL [*Rein*, 2004] and for core 003 [*Doering et al*., 2016]. All ages are given in 1000 calendar years before 1950 A.D. (abbreviated as ka B.P.).

3.3. Biogenic Opal, Particulate Carbon, and Silicon Isotope Analyses

The bSi and organic carbon (C_{org}) concentrations for core 029 originate from *Mollier-Vogel* [2012, PhD Thesis] (Table 1; for all data see supporting information Table S3). Prior to geochemical analyses the freeze-dried sediments were grounded in an agate mortar. The amount of bSi was measured according to an automated leaching method using sodium hydroxide [*DeMaster*, 1981; *Müller and Schneider*, 1993] with a precision of 1–2% (1σ). The total C_{org} content was determined by combustion of the sediment samples using a Carlo-Erba element analyzer (NA 1500). Accumulation rates (ARs) were calculated using dry bulk density (g/cm^3) and sedimentation rates (SRs; cm ka^{-1}) obtained based on the age models.

New $\delta^{30}Si$ records were produced for cores 052 and 029. For the silicon isotope measurements diatoms were extracted from the sediment by chemical (HCl and H_2O_2) and physical cleaning (11 and 32 μm sieve; heavy liquid separation with a sodium polytungstate solution set at 2.15 mg/L) as described in detail in *Ehlert et al*. [2012, 2013] and *Doering et al*. [2016]. For all samples the purity of the small diatom fraction was evaluated via light microscopy prior to dissolution and only pure (>95%) diatom samples were treated further. An exception was the 11–32 μm diatom fraction in the Holocene section of core 029 where high sponge spicule abundances ranging from 6 to 12% equivalent to 8 to 16% in biovolume have been observed (see supporting information for detailed calculation; see also supporting information Table S4). During this time period $\delta^{30}Si_{bSi}$ signatures are lighter than +0.5‰ and may have been altered by contributions of lighter sponge spicule $\delta^{30}Si_{bSi}$ which can be as low as −1‰ to −4‰ [*Hendry et al*., 2010]. To evaluate the potential contamination effect for samples of core 029 with high sponge spicule content (above 5% biovolume), we assumed $\delta^{30}Si$ values of both −1‰ and −4‰ for each sample, given that no specific $\delta^{30}Si$ signatures are available for sponges from the area off Peru. The corrected $\delta^{30}Si_{bSi}$ signatures reach values of between +0.19‰ and +0.76‰, which are well within the range of modern values at the core site, and demonstrate that the measured $\delta^{30}Si_{bSi}$ signatures are reasonable and are not fundamentally altered by sponge signatures. Other siliceous organisms, such as radiolarians or silicoflagellates accounted for less than 1% of the total sediment throughout all cores. In addition to the separation of the small diatom fraction large diatoms were handpicked from the 125/150-250 μm size fraction following *Ehlert et al*. [2012].

All diatom samples were dissolved in 1 mL 0.1 M NaOH and treated with 200 μL concentrated H_2O_2 (Suprapur). Sample solutions were diluted with 4 mL MQ water and neutralized with 0.1 mL 1 M HCl [*Reynolds et al*., 2008], followed by a chromatographic purification with 1 mL precleaned AG50W-X8 cation exchange resin (BioRad, mesh 200–400) [*de Souza et al*., 2012b]. The Si isotope ratios were determined in 0.6 ppm sample solutions on a *NuPlasma HR* MC-ICPMS at GEOMAR via a standard-sample bracketing method [*Albarède et al*., 2004]. Silicon isotope compositions are reported in the δ notation relative to the reference standard NBS28 in parts per thousand ($\delta^{30}Si = ((R_{sample}/R_{standard}) - 1) * 1000$) where R_{sample} is the $^{30}Si/^{28}Si$ ratio of the sample and $R_{standard}$ is the $^{30}Si/^{28}Si$ ratio of the NBS28. Long-term repeated measurements of the reference materials NBS28, IRMM018, and Big Batch gave average $\delta^{30}Si$ values of 0.00 ± 0.23‰ (2σ, $n = 23$), −1.44 ± 0.24‰ (2σ, $n = 21$), and −10.59 ± 0.24‰ (2σ, $n = 22$), respectively, which are in good agreement with literature values [*Reynolds et al*., 2007]. All $\delta^{30}Si$ measurements were run at least in triplicates with reproducibility (2σ; see Table 1) generally within the external reproducibility of ±0.23‰ (2σ).

3.4. Diatom Assemblage Data

The diatom assemblages were determined on the separated and cleaned 11–32 μm fractions by light microscopy (at 200–400X magnification; Figure 5; supporting information Table S4). Smear slides were prepared of every second sample, and when the amount of the sample is permitted, three transects of 300 specimens were counted. With the exception of fragments of *Coscinodiscus* spp. diatom species counts were only performed on those frustules of which at least two thirds of the frustule was preserved [*Crosta and Koç*, 2007]. The fragments of the large species were, however, all counted to estimate the contribution of the generally higher silicon isotope composition of this genus on the mixed signatures of the small-sized fraction. The abundances of three groups of diatom species representing particular environmental conditions were identified according to earlier studies off Peru [*Schuette*, 1980; *de Mendiola*, 1981; *De Vries and Schrader*, 1981; *Schuette and Schrader*, 1981; *Abrantes et al*., 2007]: (1) coastal upwelling with nutrient-rich, turbulent waters: *Chaetoceros* spp. and resting spores, *Skeletonema costatum*, *Thalassionema nitzschioides* var. *nitzschioides*; (2) coastal planktonic (temperate and cosmopolitan) with high-to-moderate nutrient waters: *Actinocyclus* spp., *Actinoptychus* spp., *Asteromphalus* spp., and *Cyclotella* spp.; and (3) other diatom species: oceanic planktonic (warm and temperate) from nutrient-depleted waters such as *Nitzschia* spp., and *Rhizosolenia* spp., as well as *Thalassiosira* spp., and benthic diatoms such as *Biddulphia* spp., *Cocconeis* spp., and *Delphineis karstenii*.

The determination of the diatom assemblages in the 11–32 μm fraction is only a qualitative simplified approach compared to the bulk sediment assemblage analyses given that the specific size range excludes smaller and larger diatom species. However, it was shown that this size range closely reflects the main assemblage composition and is suitable to contribute to the interpretation of the corresponding $\delta^{30}Si_{bSi}$ signatures [*Ehlert et al*., 2012, 2013]. Nonetheless, due to the loss of substantial amounts of small upwelling-related species associated with the 11–32 μm fraction during sample preparation, the diatom assemblage of this size

Table 2. Location and Water Depth of the Cores Used for Comparison of Opal Fluxes

No.	Core	Latitude	Longitude	Water Depth	Reference
7	RC11-238[a]	−1.517	−85.817	2573	*Bradtmiller et al.* [2006]
9	V19-30[a]	−3.383	−83.517	3091	*Bradtmiller et al.* [2006]
10	TR163-31P[a]	−3.619	−83.971	3205	*Kienast et al.* [2006]
6	ME0005-24JC[a]	0.022	−86.463	2941	*Kienast et al.* [2006]
8	ME0005-27JC[a]	−1.853	−82.787	2203	*Dubois et al.* [2010]
5	ODP202-1240A[a]	0.022	−86.463	2922	*Pichevin et al.* [2009]
1	M77/2-052[b]	−5.483	−81.45	1249	*Schönfeld et al.* [2015, this study]
2	M77/2-029[b]	−9.283	−79.617	444	*Schönfeld et al.* [2015, this study]
3	SO147-106KL[b]	−12.05	−77.667	184	*Ehlert et al.* [2013]
4	M77/2-003[b]	−15.1	−75.683	271	*Doering et al.* [2016]
11	GeoB 7112-5[b]	−24.033	−70.823	2507	*Mohtadi* [2004]
12	GeoB 7139-2[b]	−30.2	−71.983	3267	*Mohtadi* [2004]

[a]Opal fluxes were calculated via ^{230}Th normalization.
[b]Opal fluxes were calculated without ^{230}Th normalization.

fraction can only indicate approximate changes of the original assemblage and is thus only applied to assess changes in upwelling intensity.

4. Results and Discussion

The new records of cores 052 and 029 complement those already existing for bSi and C_{org} concentrations and sedimentation rates and resulting opal and organic carbon fluxes (AR_{bSi} and AR_{Corg}), $\delta^{30}Si_{bSi}$, and $\delta^{30}Si_{Coscino}$ records obtained from cores 106KL and 003 at the Peruvian margin (see Table 2 and Figures 3 and 4). We combine the four records to comprehensively evaluate latitudinal shifts and changes in the degree of nutrient utilization (based on $\delta^{30}Si_{bSi}$ and $\delta^{30}Si_{Coscino}$) together with changes in productivity and upwelling intensity (based on bSi and C_{org} and diatom assemblages; Figures 3–5). Hereby, we focus on the comparison of the present-day conditions to changes during the Holocene and T1 for the coastal upwelling area off Peru between 5°S and 15°S.

The data set demonstrates that large and systematic variations in sedimentation, productivity, nutrient utilization, and upwelling intensity occurred over time at all four sites (i.e., temporal variations). It also documents pronounced spatial differences between the different locations along the Peruvian margin. All data indicate a correspondence of intensified upwelling conditions (diatom assemblage and $\Delta^{30}Si_{Coscino\text{-}bSi}$) with elevated $\delta^{30}Si$ signatures as previously suggested for coastal upwelling systems [*Ehlert et al.*, 2013; *Pichevin et al.*, 2014; *Ehlert et al.*, 2015; *Doering et al.*, 2016]. However, we do not observe synchronous changes in productivity and upwelling intensity between T1 and the Holocene at the different core locations along the margin (i.e., spatial variations).

4.1. Regional Changes in Past Sedimentation Regimes and Productivity

In general, sedimentations rates (SRs) and bSi concentrations (wt %) covary in the records from the PUE, while the C_{org} content indicates a general increase from the glacial to the Holocene (Figure 3). Furthermore, periods of highest SR and thus ARs are associated with laminations in the sediment records. Although changes in past SRs are likely partly influenced by the hydrographic changes (velocity of PCUC, NLIWs, and bottom water oxygenation) we interpret the general trends of AR_{bSi} and AR_{Corg} records to mainly reflect changes in productivity.

Core 052, located in the northern part of the margin below the shelf break, is the only core without any distinct changes in SR. This record is characterized by overall very low SR of 20 to 27 cm ka^{-1} that results in the lowest AR_{bSi} and AR_{Corg} values of our Peruvian margin section of 0.5–1.4 g cm^{-2} ka^{-1} and 0.2–0.5 g cm^{-2} ka^{-1}, respectively.

Core 029 from 9°S at 400 m water depth is located within an area where at present only small amounts of sediment are deposited due to high-energy hydrographic conditions, such as peak velocities of the PCUC (for details see *Erdem et al.* [2016]). Hence, both the modern and Holocene SRs (11–20 cm ka^{-1}) and ARs

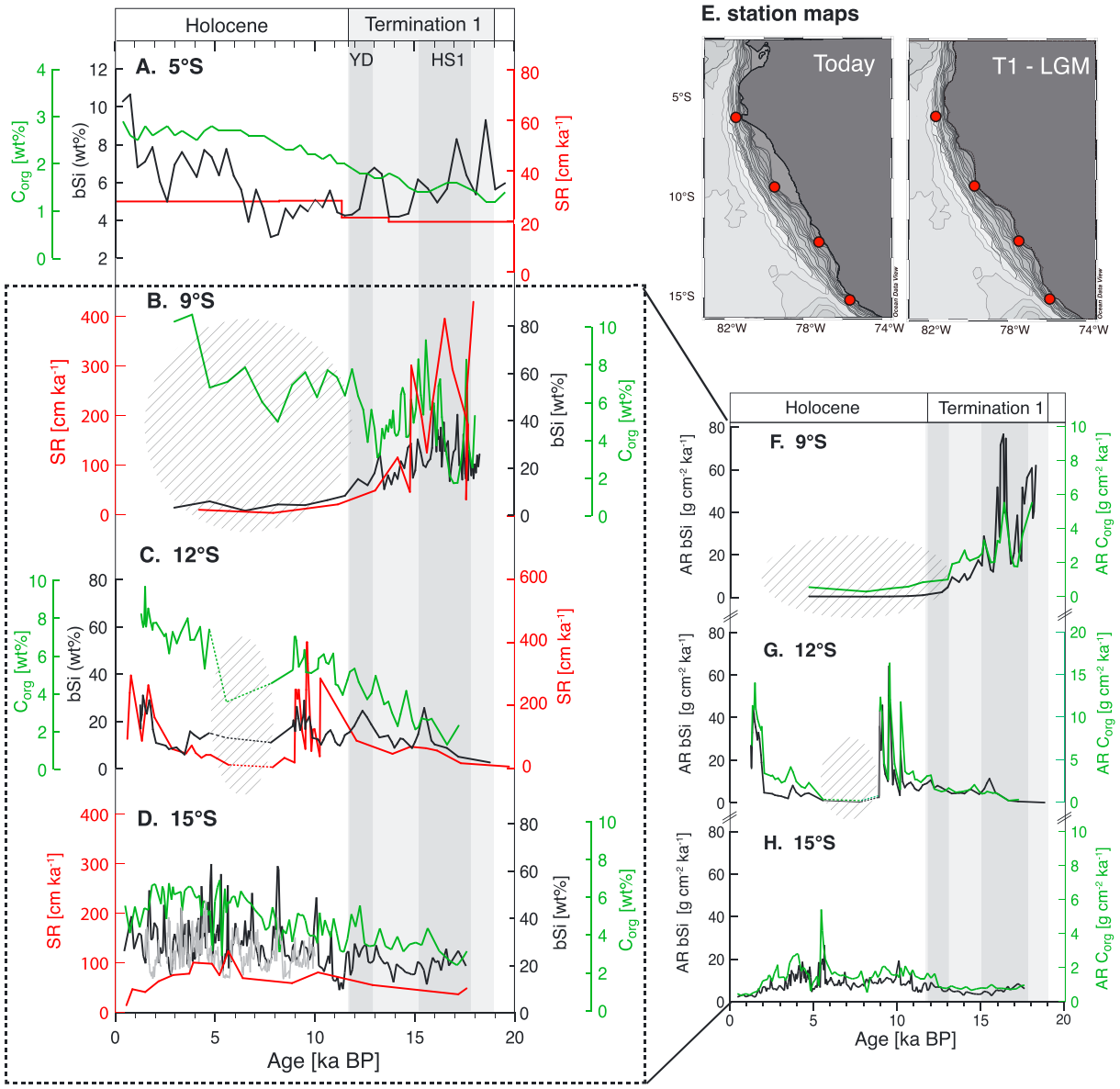

Figure 3. (a–d) Time series of SR (red lines; cm ka^{-1}), bSi content (black lines; wt %), and organic carbon content (green lines; wt %) of cores 052, 029, 106KL, and 003. Note the different scales of each core. (e) Station map today (left) and for a lower sea level during T1 and the LGM (right; based on the 120 m isoline). (f–h) Time series of accumulation rates of bSi (black lines) and organic carbon (green lines) for cores 029, 106KL, and 003. Shaded areas mark time periods characterized by either extremely low sedimentation rates, nondepositional conditions or by a hiatus in the record.

(mean AR_{bSi} value = 1.1 g cm^{-2} ka^{-1}) were relatively low (Figure 3f). In marked contrast, during T1 bottom currents were obviously less effective and not erosive, which is documented by sedimentation rates of up to 430 cm ka^{-1} at this location. The records from the southern shelf (12°S and 15°S) show substantially lower AR_{bSi} values during T1 (mean AR_{bSi} = 5.6 g cm^{-2} ka^{-1} in 106KL and 5.4 g cm^{-2} ka^{-1} in 003; Figures 3g and 3h), whereas much higher productivity prevailed at both sites during the early Holocene (max AR_{bSi} = 64 g cm^{-2} ka^{-1} for 106KL and 19 g cm^{-2} ka^{-1} for 003). At 12°S, productivity reached its highest values (AR_{bSi} 40 to 64 g cm^{-2} ka^{-1}) around 10–11 ka B.P. and around 2 ka B.P. Core 003 shows a different evolution of productivity (AR_{bSi}), with maximum values at 10 ka B.P. (19 g cm^{-2} ka^{-1}), 5.7 ka B.P. (27 g cm^{-2} ka^{-1}), and between 4.5 and 5 ka B.P. (19 g cm^{-2} ka^{-1}), a period unfortunately not covered by core 106KL, due to a hiatus between 6 and 8 ka B.P. Interestingly, after 2 ka B.P. AR_{bSi} decreased in core 003 (2 g cm^{-2} ka^{-1}) when a

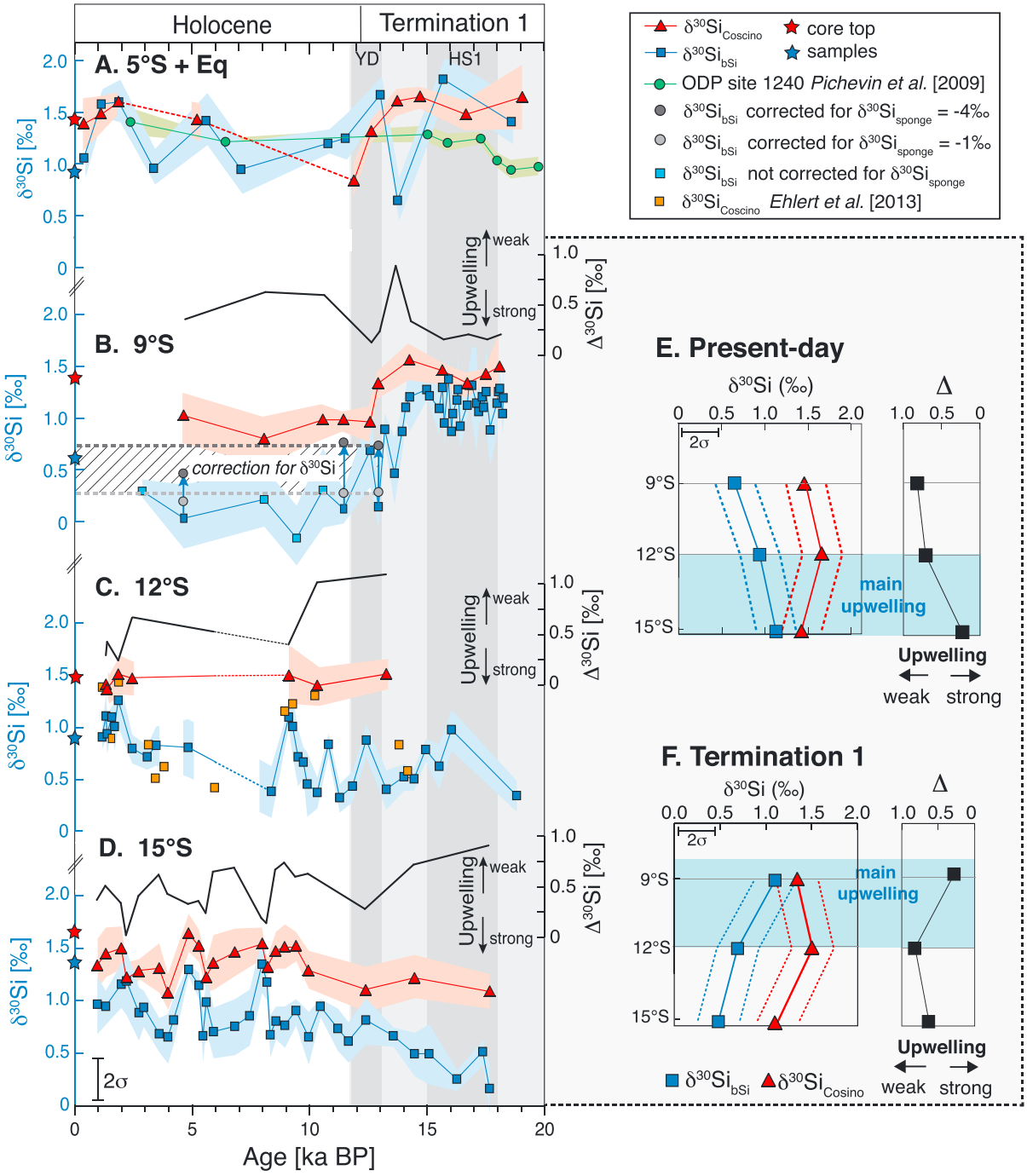

Figure 4. (a–d) Downcore records for $\delta^{30}Si_{bSi}$ (blue squares) and $\delta^{30}Si_{Coscino}$ (red triangles) signatures of cores 052, 029, 106KL, and 003 and ODP site 1240. The colored areas indicate reproducibility based on replicate measurements. The external reproducibility (2σ) is indicated as black bar. The corresponding offset $\Delta^{30}Si_{Coscino\text{-}bSi}$ (Δ) is shown as black lines. Dashed lines indicate gaps in the $\delta^{30}Si$ record due to low sedimentation rates (cores 029 and 052). The hiatus in the sedimentary record of core 106KL between 6 ka and 8 ka B.P. is marked with dotted lines. The red and blue stars mark the $\delta^{30}Si_{bSi}$ and $\delta^{30}Si_{Coscino}$ signatures of the corresponding core top samples. Heinrich Stadial 1 and the Younger Dryas are denoted by gray shading. (e, f) Latitudinal distribution of mean $\delta^{30}Si_{bSi}$ and $\delta^{30}Si_{Coscino}$ signatures and $\Delta^{30}Si_{Coscino\text{-}bSi}$ (Δ) values at 9°S, 12°S, and 15°S for present-day conditions and T1. Dashed lines indicate measurement uncertainties.

marked increase (42 g cm^{-2} ka^{-1}) was recorded in core 106KL. Overall, the variability in bSi concentrations and their general pattern during the Holocene in core 003 compares well with a record from 15°S covering the Holocene (Figure 3d, gray line) [*Chazen et al.*, 2009], confirming that core 003 provides an essentially undisturbed sediment record.

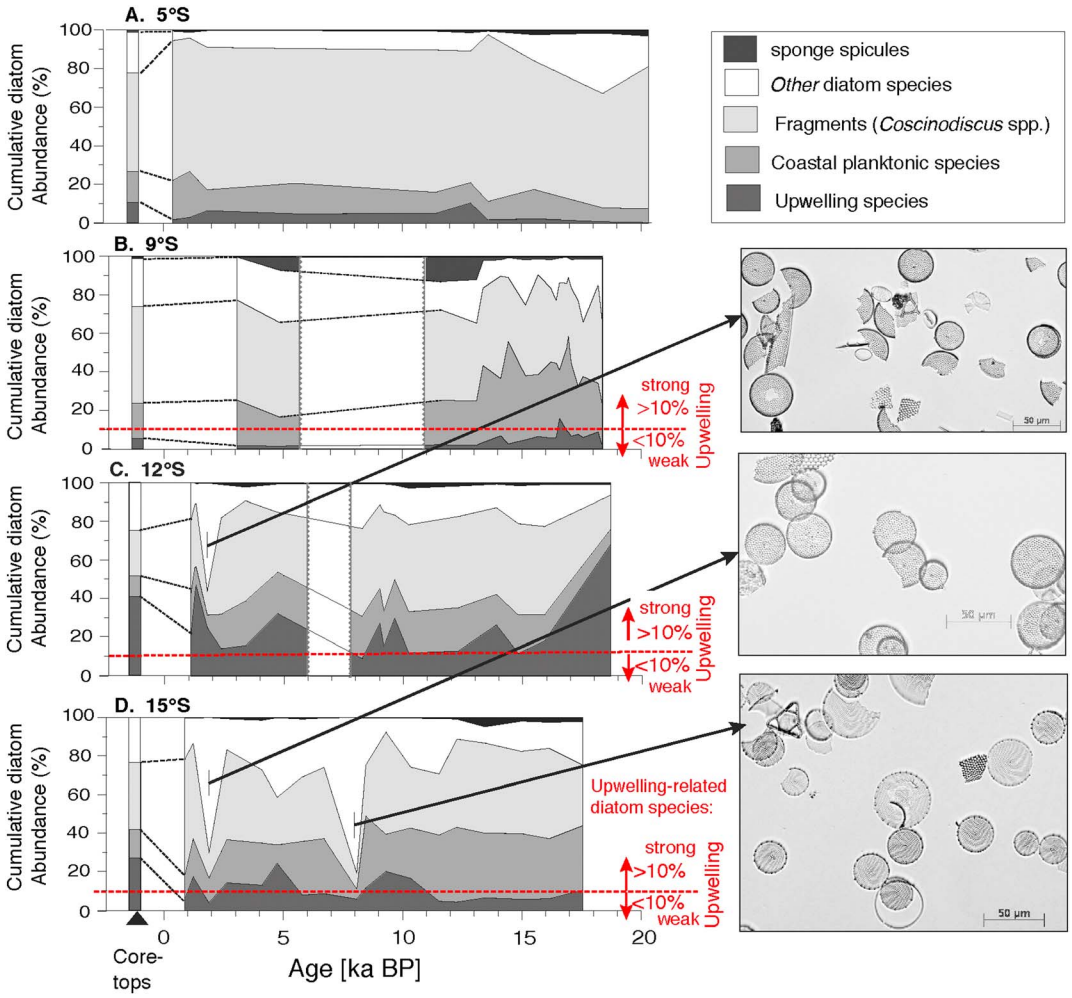

Figure 5. Cumulative diatom assemblages of cores 052, 029, 106KL, and 003; core top values are given as bar plot on the left hand-side; sponge spicules—black; other diatom species—white; *Coscinodiscus* spp. fragments—light gray; coastal planktonic species—gray; upwelling-related species—dark gray. The horizontal red dashed lines on the four records mark the 10% abundance of upwelling-related species. The microscopic images on the right side illustrate samples with a >50% contribution of other diatoms, mainly the subtropical species *Thalassiosira eccentrica* and *Azpeitia* sp.

4.2. Past Changes in Nutrient Utilization and Upwelling Intensity

In previous studies it was found that different diatom fractions represent different succession stages of blooming events and therefore are characterized by different $\delta^{30}Si$ values representing variations in Si utilization [*Ehlert et al.*, 2013; *Doering et al.*, 2016]. Hence, the difference in $\delta^{30}Si$ signatures between both size fractions ($\Delta^{30}Si$) was shown to correlate with upwelling intensity, with lowest $\Delta^{30}Si$ values (<+0.3‰) where upwelling is strongest and vice versa. In a complementary approach the upwelling intensity was determined based on the diatom assemblage of the 11–32 µm fraction [*Doering et al.*, 2016]. Accordingly, intense upwelling conditions are reflected by high abundances of upwelling-related species between 10 and 60% (Figure 5). Our new records also indicate that $\delta^{30}Si_{Coscino}$ values are in general higher than $\delta^{30}Si_{bSi}$ values of the same sample (Figure 4). The surface $\delta^{30}Si_{bSi}$ and $\delta^{30}Si_{Coscino}$ signatures of cores 029, 106KL, and 003 are generally in good agreement with distribution patterns in surface sediments [*Doering et al.*, 2016] characterized by heavier $\delta^{30}Si_{bSi}$ signatures around +1‰ and lower $\Delta^{30}Si$ (= $\delta^{30}Si_{Coscino} - \delta^{30}Si_{bSi}$) values of about +0.3‰ to +0.6‰ denoting high productivity (bSi) and upwelling intensity (abundance of upwelling-related diatoms >10%; Figure 5).

4.2.1. The Central and the Southern Shelf (9°S to 15°S) During Termination 1

Following these previous findings, the high $\delta^{30}Si_{bSi}$ signatures (+1.0 ± 0.2‰), low $\Delta^{30}Si$ values (mean value = 0.3‰; Figure 4b), and increased abundance of upwelling-related diatoms (up to 15%; Figure 5b) at 9°S during T1, associated with highest AR_{bSi} (up to 77 g cm^{-2} ka^{-1}), indicate conditions of high productivity and upwelling intensity very similar to those observed today at the southern shelf between 12°S and 15°S. Conversely, lower AR_{bSi} during T1 at 12°S and 15°S are associated with low $\delta^{30}Si_{bSi}$ values (+0.7 ± 0.3‰ core 106KL; +0.5 ± 0.2‰ core 003) and higher $\Delta^{30}Si$ values of +0.8‰ and +0.6‰, indicating less intense productivity and a significantly weakened upwelling cell at that time. Please note that mean $\Delta^{30}Si$ and $\delta^{30}Si_{Coscino}$ values of core 106KL were calculated based on new $\delta^{30}Si_{Coscino}$ data produced in this study, given that the previously published $\delta^{30}Si_{Coscino}$ signatures of that core [*Ehlert et al*., 2013] were not measured at the same sample depths as the $\delta^{30}Si_{bSi}$ signatures. The previously measured $\delta^{30}Si_{Coscino}$ values of core 106KL (Figure 4c, orange squares) [*Ehlert et al*., 2013] show a much lower mean value of +0.88 ± 0.34‰ in comparison to the signatures of the new samples and of the other cores, which are close to +1.5‰. As measurements precision and accuracy of the new and previously reported samples and standard material as well as surface sediment measurements [*Ehlert et al*., 2012; *Doering et al*., 2016] and measurements of standard reference materials (see section 3.3) were similar, we exclude a measurement artifact to cause this difference in the $\delta^{30}Si_{Coscino}$ values. Instead, it is most likely that low $\delta^{30}Si_{Coscino}$ values (+0.5‰) observed between 3 ka and 7 ka B.P., as well as at 14 ka B.P., reflect phases of weak upwelling coupled with a limitation by nutrients other than $Si(OH)_4$, which affected the diatoms. Similarly, the range of variation in $\delta^{30}Si_{bSi}$ signatures (+0.7 ± 0.3‰) is much higher than in the other cores. It is striking that this high variability is observed at 12°S, located between the areas farther north (9°S) dominated by high PP ($AR_{bSi} > 10$ g cm^{-2} ka^{-1}) and high Si utilization ($\delta^{30}Si_{bSi}$ = +1.1‰) and farther south (15°S) dominated by low PP ($AR_{bSi} < 10$ g cm^{-2} ka^{-1}) and lower Si utilization ($\delta^{30}Si_{bSi}$ = +0.5‰) during T1. However, high $\delta^{30}Si_{bSi}$ values (+1‰) are associated with high (>20%) abundances of upwelling-related diatoms, although the AR_{bSi} values remained stable at a low level (<10 g cm^{-2} ka^{-1}). Consequently, at 12°S a short-term occurrence of enhanced upwelling conditions with $\delta^{30}Si_{bSi}$ values close to +1‰ and upwelling-related diatoms >20% is not reflected by higher bSi accumulation rates to the sediment during this time interval. This may indicate that the core site was more strongly affected by local variations of the environmental forcing factors.

4.2.2. The Central and the Southern Shelf (9°S to 15°S) During the Holocene

During the Holocene at each location AR_{bSi}, $\delta^{30}Si_{bSi}$ and $\delta^{30}Si_{Coscino}$ signatures, as well as $\Delta^{30}Si$ values, shifted to their respective present-day conditions with intense upwelling conditions at the southern shelf (between 12°S and 15°S) ($AR_{bSi} > 10$ g cm^{-2} ka^{-1}, $\delta^{30}Si_{bSi}$ = +0.8 to +0.9‰, and $\Delta^{30}Si$ = 0.3 to 0.5‰) and weaker upwelling conditions toward the north at 9°S ($AR_{bSi} < 10$ g cm^{-2} ka^{-1}, $\delta^{30}Si_{bSi}$ = +0.3‰, and $\Delta^{30}Si$ = 0.7‰) (Figures 3 and 4). The above evidence is supported by a shift from laminated to nonlaminated sediments in the northern cores, hence from high productivity and oxygen-free bottom waters to low productivity and higher bottom water oxygenation (Figure 2) [*Brodie and Kemp*, 1994; *Salvatteci et al*., 2014a; *Fleury et al*., 2015; *Schönfeld et al*., 2015]. A new observation is the high abundance of *other* diatom species, mainly the subtropical groups *Thalassiosira eccentrica* and *Azpeitia* spp., at 8.2 ka and 1.9 ka B.P. in cores 106KL and 003. These high abundances likely reflect the periodical inflow of subtropical waters, potentially associated with El Niño-like conditions, at these times [*Rein et al*., 2005; *Ehlert et al*., 2013]. Interestingly, these samples also show high $\delta^{30}Si_{bSi}$ values of +1.2‰ to +1.3‰, which could reflect high Si utilization during El Niño events, which would be in contrast to lower $\delta^{30}Si_{bSi}$ values generally observed for weak upwelling conditions [*Doering et al*., 2016].

4.2.3. The Northern Peruvian Shelf (Equator to 5°S)

Unlike the other $\delta^{30}Si_{Coscino}$ records in this study, which are generally substantially heavier than the $\delta^{30}Si_{bSi}$ signatures, the $\delta^{30}Si_{bSi}$ and $\delta^{30}Si_{Coscino}$ signatures of core 052 overlap (Figure 4a). This is accompanied by high abundances of *Coscinodiscus* spp. fragments (>60%) within the 11–32 μm fraction (Figure 5a). It was not possible to measure $\delta^{30}Si_{bSi}$ and $\delta^{30}Si_{Coscino}$ values for the same samples throughout the whole core due to extremely low bSi concentrations of ~5 wt % mainly during the early and beginning of the mid-Holocene. Interestingly, both fractions exhibit signatures close to +1.5‰ along the whole record (mean $\delta^{30}Si_{bSi}$ = +1.3 ± 0.3‰ and $\delta^{30}Si_{Coscino}$ = +1.4 ± 0.2‰). This value corresponds to the present-day signatures carried by the PCUC [*Ehlert et al*., 2012], which supplies subsurface waters to the upwelling cells off Peru. The lowest values occurred during the early and mid-Holocene ($\delta^{30}Si_{bSi}$ = +1.1 ± 0.2‰; $\delta^{30}Si_{Coscino}$ = +0.8

± 0.2‰). The overlap of the $\delta^{30}Si_{bSi}$ and $\delta^{30}Si_{Coscino}$ signatures is most likely caused by the low abundance of small diatom species leading to relatively high amounts of *Coscinodiscus* fragments in the 11–32 μm fraction, which are generally associated with higher $\delta^{30}Si$ values [*Ehlert et al*., 2012, 2013; *Doering et al*., 2016]. Accordingly, any signal in the $\delta^{30}Si_{bSi}$ record reflecting changes in productivity or nutrient utilization associated with upwelling intensity is supposedly overprinted by the dominant influence of the $\delta^{30}Si_{Coscino}$ signature in the small fraction. However, the $\delta^{30}Si$ records of core 052 agree well with the record of Ocean Drilling Program (ODP) site 1240, located in the equatorial high-nitrate, low-chlorophyll area of the EEP (Figure 4a) [*Pichevin et al*., 2009; *Arellano-Torres et al*., 2011]. Accordingly, we suggest that near-complete $Si(OH)_4$ utilization and thus Si-limited conditions have prevailed in the surface waters at these two sites since HS1.

In summary, the combination of the proxy records (Figures 3, 4, and 5) allows to reconstruct past variations in Si cycling along the Peruvian margin. The comparison of $\delta^{30}Si_{bSi}$ and $\delta^{30}Si_{Coscino}$ values (Figure 4) shows that the highest nutrient utilization occurred in the northern part of the PUE (i.e., 052 and ODP site 1240) over the entire 20,000 years. Within the shelf area to the south (cores 029, 106KL, and 003) utilization has generally been lower. During T1 utilization was highest at 9°S on the shelf and decreased to the south. The Si isotope values of cores 029, 003, and 106KL only converge during the Younger Dryas (YD) indicating the shift, the main upwelling intensity, and diatom productivity to the southern sites during the early Holocene. This switch in the spatial distribution of upwelling intensity is also reflected in the record of $\Delta^{30}Si$ values. Accordingly, the $\Delta^{30}Si$ values were generally low during HS1 and the YD (+0.25‰) and high during the Holocene (+0.65‰), while only the $\Delta^{30}Si$ values of core 003 decreased from T1 to the Holocene, indicating a southward shift of the upwelling center during the Holocene (Figure 4f).

4.3. Mechanisms Driving Past PP Variability and Upwelling Intensity: Response of the Peruvian Upwelling System to Past Forcing by the Ocean-Atmosphere Circulation

Variations in productivity off Peru have mainly been driven by changes in nutrient and Fe fluxes to surface waters, which vary due to changes in upwelling intensity induced by the trade winds as well as variable nutrient concentrations in subsurface waters [*Loubere*, 1999]. Those variations in upwelling strength are expected to have been closely coupled to ocean-atmosphere circulation, which determines the position and strength of the SPSH linked to Walker circulation strength as well as to the position of the ITCZ and the Southern Westerly Wind (SWW) (Figure 1) [*Barber and Chávez*, 1983; *Strub et al*., 1998]. Variations during the late Holocene have previously been suggested to follow Northern Hemisphere warm and cold periods, with increased upwelling intensity and PP (La Niña-like mean state) occurring during warm periods and reduced upwelling and PP conditions (El Niño-like mean state) during colder periods [*Sifeddine et al*., 2008; *Gutiérrez et al*., 2009; *Salvatteci et al*., 2014b; *Ehlert et al*., 2015]. However, the regional differences in the evolution of productivity, nutrient utilization, and upwelling conditions on the Peruvian shelf between 5°S and 15°S presented here indicate that the variations observed between the LGM and today were much more complex and likely influenced by local differences between core sites.

During T1, the observed decrease in productivity and upwelling intensity at 15°S, reflected by low AR_{bSi} and $\delta^{30}Si_{bSi}$ and high $\Delta^{30}Si$ (Figures 3 and 4), is similar to the conditions reported during the LIA (1400–1850 A.D.) [*Ehlert et al*., 2015]. Such low surface productivity and upwelling intensity have been suggested to be driven by a more southerly position of the ITCZ and a weak/contracted SPSH inducing El Niño-like conditions [*Sifeddine et al*., 2008; *Gutiérrez et al*., 2009; *Sachs et al*., 2009; *Ehlert et al*., 2015]. This is consistent with interpretations based on EEP records for HS1 during T1 (Figure 6b) [*Dubois et al*., 2011; *Kienast et al*., 2013]. In contrast, at the same time, productivity and upwelling intensity were highly variable at 12°S and do not seem to follow any specific driving mechanism (such as ITCZ movement or SPSH strength; see section 4.2). However, upwelling intensity and productivity are highly dependent on the shape of the coastline and shelf depth. As the sea level was up to 120 m below its present level [*Fairbanks*, 1989] prior to 10 ka B.P. the shape of the coastline was different, thus potentially causing shifts of the upwelling centers to different locations (Figure 3e). Furthermore, core 106KL (12°S) was accordingly located in water depths as shallow as 60 m during T1 and turbulence in this near-shore area may periodically have been too intense to allow high surface productivity [*Margalef*, 1978]. The particular shape of the shoreline at 15°S to 16°S today also promotes strong coastal eddy formation leading to high near-shore productivity [*Altabet et al*., 2012; *Stramma et al*., 2013], which might have been absent during T1. Hence, sea level-driven variations of the coastline at this location

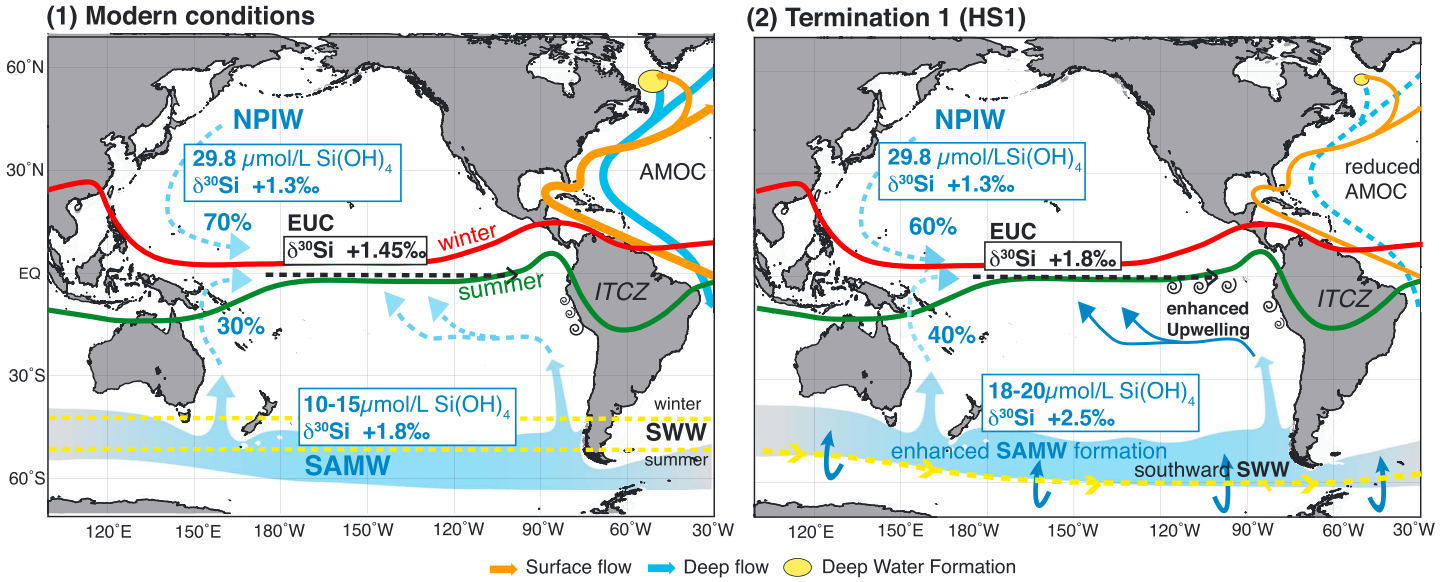

Figure 6. Schematic illustration of oceanic and atmospheric conditions prevailing (a) during modern conditions and (b) during Termination 1 (HS1) (modified from *Dubois et al.* [2011]). Modern silicon isotope signatures and dissolved silicate concentrations for NPIW and SAMW were taken from *de Souza et al.* [2012a]; the data for the SAMW during HS1 were taken from *Robinson et al.* [2014].

in the past may have significantly affected the record, which, however, remains to be verified through a dedicated modeling study and is beyond the scope of this study.

Altogether, during T1, the moderate to high $\delta^{30}Si_{bSi}$ signatures at 9°S and 12°S as well as low $\Delta^{30}Si$ values and diatom assemblages with a considerable (>10%) amount of upwelling-related species clearly indicate that at least moderate to strong upwelling conditions were maintained in this area of the Peruvian margin all the time. Similar observations were previously made based on diatom assemblage records [*De Vries and Schrader*, 1981] and molecular organic geochemical proxies [*Makou et al.*, 2010] at 11°S, both indicating continuously strong or at least moderate upwelling conditions during T1. Nevertheless, upwelling intensity and diatom productivity were substantially lower at 15°S (core 003) at the same time, suggesting a spatial shift in the main upwelling center from its modern location between 12°S and 15°S to 9°S and 12°S during T1. However, such a spatial shift in the main upwelling center is neither in agreement with a La Niña-like mean state, which should be accompanied by intense SE trade winds promoting upwelling along the whole margin, nor with an El Niño-like mean state which should cause low productivity along the whole area.

Prevailing high productivity and intense upwelling at 9°S after the LGM and at the onset of HS1 correlates with high bSi fluxes in the Southern Ocean [*Anderson et al.*, 2009], the equatorial Pacific (Figure 7a) [*Bradtmiller et al.*, 2006; *M. Kienast et al.*, 2006; *Dubois et al.*, 2010; *Hayes et al.*, 2011], and at the Chilean Coast (Figures 7e and 7f) [*Mohtadi*, 2004] between 10 ka and 15 ka B.P. The high productivity at the southern Chilean coast between 24°S and 30°S was suggested to be caused by a northerly position of the SWW and the Antarctic Circumpolar Current during the LGM (Figures 7e and 7f) [*Mohtadi*, 2004]. This also enhanced vertical mixing in the Southern Ocean, leading to an increase in bSi production south of the Antarctic Polar Front during Antarctic warming between approximately 10 ka and 15 ka B.P. (concomitant with HS1; Figure 6b) [*Toggweiler et al.*, 2006; *Anderson et al.*, 2009; *Hendry and Brzezinski*, 2014]. These records are consistent with a more northward position of the main upwelling center at 9°S off Peru (Figure 4f), which likely occurred in response to the northward shift of the SWW and SPSH during the LGM followed by a transient southward shift during T1.

Based on the increased ventilation and enhanced surface productivity accompanied by a decrease in dust transport to the Southern Ocean, it was proposed that the increased formation of intermediate waters promoted the export of $Si(OH)_4$ to the low latitudes between 10 ka and 15 ka B.P. [*Anderson et al.*, 2009; *Hayes et al.*, 2011; *Pena et al.*, 2013; *Hendry and Brzezinski*, 2014], which may also potentially have stimulated diatom

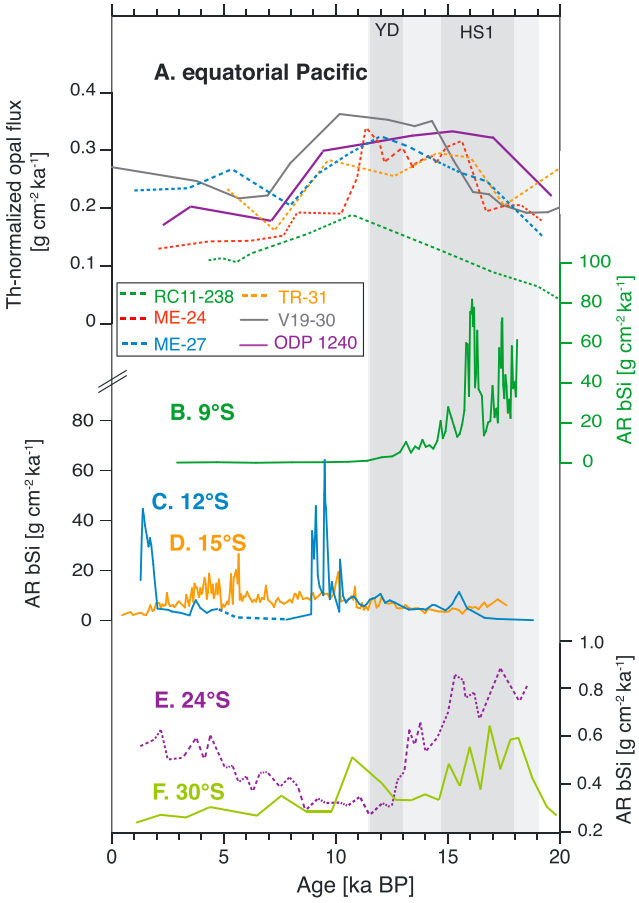

Figure 7. Downcore comparison of bSi fluxes from (a) the EEP [*Bradtmiller et al*., 2006; *S. S. Kienast et al*., 2006; *Pichevin et al*., 2009; *Dubois et al*., 2010], (b–d) the PUE [*Ehlert et al*., 2013; *Schönfeld et al*., 2015; *Doering et al*., 2016, this study], and (e, f) the Chilean Coast [*Mohtadi*, 2004] for the past 20 ka. Accumulation rates for the EEP and the Southern Chilean Coast are given as ^{230}Th-normalized bSi fluxes, while the records from the PUE and Northern Chilean Coast were calculated without ^{230}Th normalization and were calculated from bSi content, SRs, and DBD.

bSi PP in these regions. This is supported by records from the equatorial Pacific indicating high (^{230}Th normalized) bSi fluxes during T1, which strongly increase at the onset of HS1 (Figure 7a) [*Bradtmiller et al*., 2006; *M. Kienast et al*., 2006; *Dubois et al*., 2010; *Hayes et al*., 2011]. Increased nutrient supply to the EEP may have lifted the colimitation of surface productivity by $Si(OH)_4$ and Fe. In addition, based on alkenone paleothermometry, *Dubois et al*. [2011] and *Kienast et al*. [2013] proposed an increase in equatorial upwelling intensity to explain the doubling of export production in the equatorial Pacific during T1 [*Hayes et al*., 2011]. This increase was due to the enhancement of the NE trade winds as a consequence of a reduction in AMOC strength and hence intensification of the Central American gap wind system associated with the southward migration of the ITCZ during HS1. However, other studies favor a strengthened upwelling, thermocline shoaling, and increased equatorial productivity due to a La Niña-like mean state accompanied by an increase in SE trade winds as the main causes for the changes observed [*Pena et al*., 2008; *bin Shaari et al*., 2013]. In comparison to the evolution in bSi productivity in the equatorial Pacific during HS1, productivity did not increase during T1 at the northern shelf edge (5°S). Instead, the record rather indicates a decrease in upwelling intensity. Given that this location (5°S) is generally unaffected by the influence of strong coastal upwelling, regardless of the position of the upwelling cell, we can exclude a strong impact of changing nutrient supply, for example, via the EUC to the PCUC. This is in agreement with a nearby record at 3.5°S, where the enhanced influence of upwelled waters from the south was also not observed prior to 4 ka B.P. [*Nürnberg et al*., 2015]. Moreover, the high sedimentation rates and laminations observed at the central shelf (9°S) indicate a substantial decrease in current velocities and a shift in the hydrographic system at the onset of T1. Such a change may either be the result of an enhanced La Niña-like mean state [*Montes et al*., 2011] or could be explained by a weaker seasonal SST contrast and inferred decrease in EUC velocities during T1 [*Nürnberg et al*., 2015].

Overall, the combined records of AR_{bSi}, $\delta^{30}Si_{bSi}$ values, and diatom assemblages suggest that the onset of T1 was characterized by moderate upwelling and productivity between 9°S and 12°S, markedly different from modern conditions due to the more northern position of SWW and the SPSH. Southeasterly trade winds do not seem to have intensified as the coastal cold tongue did not expand farther north, which is in agreement with reports of a potentially weaker ITCZ during the LGM [*McGee et al*., 2014]. With the onset of HS1, a southward shift in the mean position of the ITCZ and the associated strengthening of the NE trade winds,

Table 3. Parameters Used for Water Mass Mixing Calculations of Northern and Southern Source Waters Contributing to the EUC[a]

	Modern			Termination 1		
	f (Si Flux)	$Si(OH)_4$ (μmol/kg)	$\delta^{30}Si$ (‰)	*f* (Si Flux)	$Si(OH)_4$ (μmol/kg)	$\delta^{30}Si$ (‰)
NPIW	0.69[b]	29.8[b]	+1.3	0.58	29.8[b]	+1.3
SAMW	0.31[b]	11.5[b]	+1.8	0.42	19	+2.5
Calculated EUC		24.3	**+1.45**		25.5	**+1.8**

[a]Calculated $\delta_{30}Si$ values are highlighted in bold.
[b]Values from *Dugdale et al.* [2002].

causing a regional increase in equatorial upwelling [*Dubois et al*., 2011; *Kienast et al*., 2013], are consistent with the continuous decrease in upwelling intensity, productivity, and nutrient utilization at 9°S as well as with prevailing low productivity and upwelling intensity at 15°S. Accordingly, the southward movement of the ITCZ is in accordance with reconstructions of enhanced river runoff from northern Peru at this time period [*Mollier-Vogel et al*., 2013]. Modern conditions characterized by increased productivity and upwelling along the southern shelf were thus only established during the early Holocene after the YD. Ultimately, our reconstructions and comparison of past diatom productivity and upwelling conditions off Peru do not indicate shifts simply following El Niño- or La Niña-like mean states as neither the seasonal (Figure 1) nor interannual (i.e., ENSO) modern variability can explain the observed changes. This is in agreement with previous observations from the California upwelling system [*McClymont et al*., 2012] and rather supports a connection to shifts in the position of the ITCZ and SWW, affecting the SPSH. Accordingly, this would support studies from the equatorial Pacific indicating a southward shift of the ITCZ and upwelling induced by NE trade winds strengthened by a reduction of the AMOC (Figure 6b) [*Kienast et al*., 2013; *Dubois et al*., 2014].

However, while changes in atmospheric and oceanic circulation control the amount of productivity and upwelling intensity, nutrient concentrations and isotopic compositions of subsurface waters might be independently controlled by preformed seawater $\delta^{30}Si$ signatures and $Si(OH)_4$ concentrations delivered to the PCUC linked to changes in Southern Ocean ventilation and productivity.

4.4. Potential Changes in Nutrient Concentrations and Isotopic Signatures of Upwelled Source Waters

Dissolved seawater $\delta^{30}Si$ signals, apart from utilization, are influenced by the mixing of water masses [*Reynolds et al*., 2008; *Fripiat et al*., 2011]. The subsurface $\delta^{30}Si$ distribution along the Peruvian margin was shown to record a combination of preformed seawater $\delta^{30}Si$ signal and addition of a lower $\delta^{30}Si$ signal originating from remineralization [*de Souza et al*., 2012a; *Grasse et al*., 2016]. Accordingly, the observed variations in the past $\delta^{30}Si_{bSi}$ and $\delta^{30}Si_{Coscino}$ records should also reflect possible changes in the preformed seawater $\delta^{30}Si$.

4.4.1. Modern Source Water Contributions and Compositions Along the Peruvian Shelf

The upwelling of the nutrient-rich PCUC along the Peruvian margin induces high productivity in surface waters. These nutrients are delivered to the PCUC via the EUC, sSSCC, pSSCC, and by remineralized $Si(OH)_4$ along the Peruvian margin [*de Souza et al*., 2012a; *Grasse et al*., 2013]. The modern EUC is composed of southern (Sub-Antarctic Mode Water; SAMW) and northern sourced (North Pacific Intermediate Water; NPIW) water masses, whereby the southern source supplies about 30% and the northern one contributes 70% of the dissolved $Si(OH)_4$ [*Dugdale et al*., 2002]. In consistency with this observation it has previously been shown that the SAMW is characterized by highly dissolved $\delta^{30}Si$ signature of +1.8‰ and $Si(OH)_4$ concentrations of 10–15 μ*M* (Figure 6 and Table 3) [*Cardinal et al*., 2005, 2007; *Hendry et al*., 2010; *de Souza et al*., 2012a]. The NPIW is characterized by higher silicate concentrations around 30 μ*M* [*Dugdale et al*., 2002] and a lower $\delta^{30}Si$ signature of +1.3‰ [*Reynolds et al*., 2006]. Calculations of conservative mixing between these two sources lead to a dissolved $Si(OH)_4$ concentration of 24 μ*M* and a $\delta^{30}Si$ signature of +1.45‰ for the EUC (Table 3). This is in agreement with the observed seawater $\delta^{30}Si$ signatures for the EUC of +1.5 ± 0.2‰ [*Grasse et al*., 2013].

4.4.2. Influence of Variations in Past Source Water $Si(OH)_4$ and $\delta^{30}Si$

The available bSi-based evidence from the Southern Ocean indicates that there were major ecological changes on glacial-interglacial timescales, which have led to a change in the composition of southern sourced intermediate waters (for simplification we will refer only to SAMW in the following) (Figure 6).

During HS1, prolonged Fe supply, the breakdown of the glacial stratification [*Bostock et al*., 2004], and increased upwelling around Antarctica [*Anderson et al*., 2009] led to the efficient ventilation of intermediate and deep waters. Such an increase in upwelling strength is thought to have resulted in an increase in both Si and Fe supply to surface waters and the formation of SAMW with higher silicate concentrations (Silicic Acid Ventilation Hypothesis) [*Hendry and Brzezinski*, 2014], which was then advected to low latitudes, where it potentially controlled productivity in the equatorial Pacific as well as along the Peruvian margin via ocean tunneling. In a recent study *Robinson et al*. [2014] estimated much higher δ^{30}Si values of dissolved silica of approximately +2.5‰ and increased concentrations of 18–20 μM for SAMW during HS1 ($22 \pm 6\ \mu M$) [*Rousseau et al*., 2016].

Although a robust quantitative estimation of the relative contributions of southern versus northern Pacific source waters during T1 is not possible based on our data, an increase in supply from the south is very likely according to the existing published data. To evaluate the potential influence via a change in the preformed seawater δ^{30}Si, we used $Si(OH)_4$ concentrations, flow, and fluxes of the EUC as reported previously by *Dugdale et al*. [2002]. Following the approach of *Hayes et al*. [2011], we assumed NPIW as the only northern source and SAMW as the only southern source of nutrients to the EUC (Table 3). During HS1 the estimated change in $Si(OH)_4$ flux from the south results in an increase to 42% from SAMW and reduces the contribution of NPIW to 58% (Figure 6b and Table 3), assuming no change in the northern source. This calculation is consistent with observations based on δ^{13}C and ε_{Nd} records from the EEP during this time interval [*Spero*, 2002; *Pena et al*., 2008; *Hayes et al*., 2011; *Pena et al*., 2013]. At the same time the dissolved $Si(OH)_4$ concentration of the EUC would increase by only 1.2 μmol/kg (difference between modern and T1 calculated $Si(OH)_4$ concentration; Table 3). Furthermore, due to the proposed increase in the seawater δ^{30}Si signature of SAMW to +2.5‰, our calculation gives a seawater δ^{30}Si signature of the EUC of +1.8‰ during HS1, which is 0.35‰ higher than the calculated modern value (+1.45‰; Table 3). As the EUC (and the SSCCs) contributes about 30% of the volume transported to the PCUC, the seawater δ^{30}Si signature would have increased by as much as 0.17‰ based on our calculation. This small potential alteration of the subsurface water δ^{30}Si signature is in agreement with our $\delta^{30}Si_{Coscino}$ records of cores 052 and 029, which are still within the range of the modern +1.5‰ signature. Moreover, a small increase in the δ^{30}Si signature of the PCUC by approximately 0.2‰ is consistent with the data given that the $\delta^{30}Si_{Coscino}$ values of core 052 during T1 are similar to those of the late Holocene. This suggests near-complete Si utilization, despite that weaker upwelling is indicated by lower amounts of *Chaetoceros* spp. Similarly, in core 029 the $\delta^{30}Si_{bSi}$ signatures reach comparable to modern values (+1‰) and Holocene values on the southern shelf (+1‰) but do not indicate a correspondingly strong increase in upwelling-related diatoms. Accordingly, given the only minor of about 0.2‰ for the preformed $\delta^{30}Si(OH)_4$ signature in the PCUC during HS1 and no significant change in the $\delta^{30}Si_{Coscino}$ records at 9°S at T1, we rule out a large influence silicon isotope records off Peru at that time.

5. Conclusions

In this study we present two new records of bSi fluxes, δ^{30}Si signatures and diatom assemblages. We combine these new records with two previously reported records to reconstruct the variations of PP and nutrient utilization along the entire Peruvian margin for the past 20,000 years, which have responded to changes in atmospheric and oceanographic circulation since the LGM.

At the transition between the LGM and T1, productivity and utilization were markedly higher on the central shelf between 9°S and 12°S, indicating a slower PCUC and more intense upwelling conditions. At the same time, the southern shelf was characterized by low sedimentation rates, productivity, and upwelling intensity, most likely indicating a northward shift of the main upwelling center as a consequence of a southward shift of the ITCZ and the SWW belt. Although shifts in the past PUE could be coupled to general variations in ocean-atmosphere circulation (such as ITCZ and SWW position) reported for the Pacific during the last glacial-interglacial transition, changes observed during T1 do not strictly coincide with alternating El Niño- or La Niña-like mean states and are also affected by local factors along the coast such as coastline morphology and sea level change. In contrast, Holocene productivity generally ranged between moderate and high values at the southern shelf, while low or interrupted sedimentation at the central shelf and near-complete $Si(OH)_4$ utilization and more stratified conditions characterized the northern region, similar to modern conditions.

Based on our data, we were also able to estimate the influence in past variations in preformed $Si(OH)_4$ supply and accompanying seawater $\delta^{30}Si$ on the preserved diatom $\delta^{30}Si$ signatures. The results suggest an only a slight increase in seawater $\delta^{30}Si$ of the PCUC at maximum 0.17‰, which is currently not resolvable in paleoceanographic records. Such a small alteration of past seawater $\delta^{30}Si$ signature is in agreement with our $\delta^{30}Si_{Coscino}$ records, which do not indicate a substantial increase in $\delta^{30}Si$ of the source waters. However, the contribution of a slightly increased preformed seawater $\delta^{30}Si$ signature of the dissolved silicate supplied to the PCUC during T1 may still have contributed to the pronounced zonal difference observed in our $\delta^{30}Si_{bSi}$ records along the Peruvian margin.

Acknowledgments
This work is a contribution of the Collaborative Research Project 754 "Climate-Biogeochemistry interactions in the Tropical Ocean" (www.sfb754.de), which is supported by the Deutsche Forschungsgemeinschaft (DFG). Supporting information associated with this article can be found in the online version. The data of this study are available electronically at the PANGEA® Data Publisher for Earth and Environmental Science (http://www.pangea.de).

References

Abrantes, F., C. Lopes, A. Mix, and N. Pisias (2007), Diatoms in Southeast Pacific surface sediments reflect environmental properties, *Quat. Sci. Rev.*, *26*(1–2), 155–169, doi:10.1016/j.quascirev.2006.02.022.

Adler, R. F. et al. (2003), The Version-2 Global Precipitation Climatology Project (GPCP) Monthly Precipitation Analysis (1979–Present), *J. Hydrometeor*, *4*(6), 1147–1167, doi:10.1175/1525-7541(2003)004<1147:TVGPCP>2.0.CO;2.

Albarède, F., P. Telouk, J. Blichert-Toft, M. Boyet, A. Agranier, and B. Nelson (2004), Precise and accurate isotopic measurements using multiple-collector ICPMS, *Geochim. Cosmochim. Acta*, *68*(12), 2725–2744, doi:10.1016/j.gca.2003.11.024.

Altabet, M. A., E. Ryabenko, L. Stramma, D. W. R. Wallace, M. Frank, P. Grasse, and G. Lavik (2012), An eddy-stimulated hotspot for fixed nitrogen-loss from the Peru oxygen minimum zone, *Biogeosci. Discuss.*, *9*(12), 8013–8038, doi:10.5194/bgd-9-8013-2012.

Anderson, R. F., S. Ali, L. I. Bradtmiller, S. H. H. Nielsen, M. Q. Fleisher, B. E. Anderson, and L. H. Burcklele (2009), Wind-driven upwelling in the Southern Ocean and the deglacial rise in atmospheric CO_2, *Science*, *323*(5920), 1443–1448, doi:10.1126/science.1167441.

Arellano-Torres, E., L. E. Pichevin, and R. S. Ganeshram (2011), High-resolution opal records from the eastern tropical Pacific provide evidence for silicic acid leakage from HNLC regions during glacial periods, *Quat. Sci. Rev.*, *30*, 1112–1121.

Barber, R. T., and F. P. Chávez (1983), Biological consequences of El Niño, *Science*, *222*(4629), 1203–1210, doi:10.1126/science.222.4629.1203.

Beucher, C. P., M. A. Brzezinski, and J. L. Jones (2008), Sources and biological fractionation of silicon isotopes in the Eastern Equatorial Pacific, *Geochim. Cosmochim. Acta*, *72*(13), 3063–3073, doi:10.1016/j.gca.2008.04.021.

Beucher, C. P., M. A. Brzezinski, and J. L. Jones (2011), Mechanisms controlling silicon isotope distribution in the Eastern Equatorial Pacific, *Geochim. Cosmochim. Acta*, *75*(15), 4286–4294, doi:10.1016/j.gca.2011.05.024.

bin Shaari, H., M. Yamamoto, and T. Irino (2013), Enhanced upwelling in the eastern equatorial Pacific at the last five glacial terminations, *Palaeogeogr. Palaeoclimatol. Palaeoecol.*, *386*, 8–15, doi:10.1016/j.palaeo.2013.03.022.

Blaauw, M. (2010), Methods and code for 'classical' age-modelling of radiocarbon sequences, *Quat. Geochronol.*, *5*(5), 512–518, doi:10.1016/j.quageo.2010.01.002.

Blasco, D. (1971), Compsición y distribución del fitoplancton en la región del afliamiento de las costas peruanas, *Invest. Pesq.*, *35*(1), 61–112.

Bostock, H. C., B. N. Opdyke, M. K. Gagan, and L. K. Fifield (2004), Carbon isotope evidence for changes in Antarctic Intermediate Water circulation and ocean ventilation in the southwest Pacific during the last deglaciation, *Paleoceanography*, *19*, PA4013, doi:10.1029/2004PA001047.

Bradtmiller, L. I., R. F. Anderson, M. Q. Fleisher, and L. H. Burckle (2006), Diatom productivity in the equatorial Pacific Ocean from the last glacial period to the present: A test of the silicic acid leakage hypothesis, *Paleoceanography*, *21*, PA4201, doi:10.1029/2006PA001282.

Brink, K. H., D. Halpern, A. Huyer, and R. L. Smith (1983), The physical-environment of the Peruvian upwelling system, *Prog. Oceanogr.*, *12*(3), 285–305.

Brodie, I., and A. Kemp (1994), Variation in biogenic and detrital fluxes and formation of laminae in late Quaternary sediments from the Peruvian coastal upwelling zone, *Mar. Geol.*, *116*, 385–398.

Bruland, K. W., E. L. Rue, G. J. Smith, and G. R. DiTullio (2005), Iron, macronutrients and diatom blooms in the Peru upwelling regime: Brown and blue waters of Peru, *Mar. Chem.*, *93*(2–4), 81–103, doi:10.1016/j.marchem.2004.06.011.

Cane, M. A. (2005), The evolution of El Niño, past and future, *Earth Planet. Sci. Lett.*, *230*(3–4), 227–240, doi:10.1016/j.epsl.2004.12.003.

Cardinal, D., L. Y. Alleman, F. Dehairs, N. Savoye, T. W. Trull, and L. André (2005), Relevance of silicon isotopes to Si-nutrient utilization and Si-source assessment in Antarctic waters, *Global Biogeochem. Cycles*, *19*, GB2007, doi:10.1029/2004GB002364.

Cardinal, D., N. Savoye, T. W. Trull, F. Dehairs, E. E. Kopczynska, F. Fripiat, J.-L. Tison, and L. André (2007), Silicon isotopes in spring Southern Ocean diatoms: Large zonal changes despite homogeneity among size fractions, *Mar. Chem.*, *106*(1–2), 46–62, doi:10.1016/j.marchem.2006.04.006.

Chavez, F. P. (1989), Size distribution of phytoplankton in the central and eastern tropical Pacific, *Global Biogeochem. Cycles*, *3*, 27–35, doi:10.1029/GB003i001p00027.

Chavez, F. P., and R. T. Barber (1987), An estimate of new production in the equatorial Pacific, *Deep Sea Res., Part A*, *34*(7), 1229–1243, doi:10.1016/0198-0149(87)90073-2.

Chazen, C. R., M. A. Altabet, and T. D. Herbert (2009), Abrupt mid-Holocene onset of centennial-scale climate variability on the Peru-Chile Margin, *Geophys. Res. Lett.*, *36*, L18704, doi:10.1029/2009GL039749.

Chelton, D. B., S. K. Esbensen, M. G. Schlax, N. Thum, M. H. Freilich, F. J. Wentz, C. L. Gentemann, M. J. McPhaden, and P. S. Schopf (2001), Observations of coupling between surface wind stress and sea surface temperature in the eastern tropical Pacific, *J. Clim.*, *14*(7), 1–20, doi:10.1175/1520-0442(2001)014<1479:oocbsw>2.0.co;2.

Crosta, X., and N. Koç (2007), Diatoms: From micropaleontology to isotope geochemistry, in *Methods in Late Cenozoic Paleoceanography*, edited by C. Hilaire-Marcel, pp. 327–369, Elsevier, Amsterdam.

DeMaster, D. J. (1981), The supply and accumulation of silica in the marine-environment, *Geochim. Cosmochim. Acta*, *45*(10), 1715–1732.

de Mendiola, B. R. (1981), Seasonal phytoplankton distribution along the Peruvian coast, in *Coastal Upwelling*, vol. 1, pp. 348–356, AGU, Washington, D. C.

de Souza, G. F., B. C. Reynolds, G. C. Johnson, J. L. Bullister, and B. Bourdon (2012a), Silicon stable isotope distribution traces Southern Ocean export of Si to the eastern South Pacific thermocline, *Biogeosciences*, *9*(11), 4199–4213, doi:10.5194/bg-9-4199-2012-supplement.

de Souza, G. F., B. C. Reynolds, J. Rickli, M. Frank, M. A. Saito, L. J. A. Gerringa, and B. Bourdon (2012b), Southern Ocean control of silicon stable isotope distribution in the deep Atlantic Ocean, *Global Biogeochem. Cycles*, *26*, GB2035, doi:10.1029/2011GB004141.

De Vries, T. J., and H. Schrader (1981), Variation of upwelling/oceanic conditions during the latest Pleistocene through Holocene off the central Peruvian coast: A diatom record, *Mar. Micropaleontol.*, *6*(2), 157–167.
DiTullio, G. R., M. E. Geesey, J. M. Maucher, and M. B. Alm (2005), Influence of iron on algal community composition and physiological status in the Peru upwelling system, *Limnol. Oceanogr.*, *50*(6), 1887–1907.
Doering, K., C. Ehlert, P. Grasse, X. Crosta, S. Fleury, M. Frank, and R. Schneider (2016), Differences between mono-generic and mixed diatom silicon isotope compositions trace present and past nutrient utilisation off Peru, *Geochim. Cosmochim. Acta*, *177*, 30–47, doi:10.1016/j.gca.2015.12.029.
Dubois, N., M. Kienast, S. Kienast, S. E. Calvert, R. François, and R. F. Anderson (2010), Sedimentary opal records in the eastern equatorial Pacific: It is not all about leakage, *Global Biogeochem. Cycles*, *24*, GB4020, doi:10.1029/2010GB003821.
Dubois, N., M. Kienast, S. Kienast, C. Normandeau, S. E. Calvert, T. D. Herbert, and A. Mix (2011), Millennial-scale variations in hydrography and biogeochemistry in the Eastern Equatorial Pacific over the last 100 kyr, *Quat. Sci. Rev.*, *30*(1), 210–223, doi:10.1016/j.quascirev.2010.10.012.
Dubois, N., M. Kienast, S. S. Kienast, and A. Timmermann (2014), Millennial-scale Atlantic/East Pacific sea surface temperature linkages during the last 100,000 years, *Earth Planet. Sci. Lett.*, *396*, 134–142, doi:10.1016/j.epsl.2014.04.008.
Dugdale, R. C., A. G. Wischmeyer, F. P. Wilkerson, R. T. Barber, F. Chai, M. S. Jiang, and T. H. Peng (2002), Meridional asymmetry of source nutrients to the equatorial Pacific upwelling ecosystem and its potential impact on ocean-atmosphere $CO_{(2)}$ flux: A data and modeling approach, *Deep Sea Res., Part II*, *49*(13–14), 2513–2531.
Ehlert, C., P. Grasse, E. Mollier-Vogel, T. Böschen, J. Franz, G. F. de Souza, B. C. Reynolds, L. Stramma, and M. Frank (2012), Factors controlling the silicon isotope distribution in waters and surface sediments of the Peruvian coastal upwelling, *Geochim. Cosmochim. Acta*, *99*, 128–145, doi:10.1016/j.gca.2012.09.038.
Ehlert, C., P. Grasse, and M. Frank (2013), Changes in silicate utilisation and upwelling intensity off Peru since the Last Glacial Maximum—Insights from silicon and neodymium isotopes, *Quat. Sci. Rev.*, *72*, 18–35, doi:10.1016/j.quascirev.2013.04.013.
Ehlert, C., P. Grasse, D. Gutiérrez, R. Salvatteci, and M. Frank (2015), Nutrient utilisation and weathering inputs in the Peruvian upwelling region since the Little Ice Age, *Clim. Past*, *11*(2), 187–202, doi:10.5194/cp-11-187-2015-supplement.
EPICA Community Members (2006), One-to-one coupling of glacial climate variability in Greenland and Antarctica, *Nature*, *444*(7116), 195–198, doi:10.1038/nature05301.
Erdem, Z., J. Schönfeld, N. Block, and A. Eisenhauer (2016), Peruvian sediments as recorders of an evolving hiatus for the last 22 thousand years, *Quat. Sci. Rev.*, *137*, 1–14, doi:10.1016/j.quascirev.2016.01.029.
Estrada, M., and D. Blasco (1985), *Phytoplankton Assemblages in Coastal Upwelling Areas*, edited by C. Bas et al., Inst. de Invest. Pesqueras, Barcelona.
Fairbanks, R. G. (1989), A 17, 000-year glacio-eustatic sea level record: Influence of glacial melting rates on the Younger Dryas event and deep-ocean circulation, *Nature*, *342*(6250), 637–642, doi:10.1038/342637a0.
Fiedler, P. C., and L. D. Talley (2006), Hydrography of the eastern tropical Pacific: A review, *Prog. Oceanogr.*, *69*(2–4), 143–180, doi:10.1016/j.pocean.2006.03.008.
Fleury, S., P. Martinez, X. Crosta, K. Charlier, I. Billy, V. Hanquiez, T. Blanz, and R. R. Schneider (2015), Pervasive multidecadal variations in productivity within the Peruvian Upwelling System over the last millennium, *Quat. Sci. Rev.*, *125*(C), 78–90, doi:10.1016/j.quascirev.2015.08.006.
Fripiat, F., A.-J. Cavagna, N. Savoye, F. Dehairs, L. André, and D. Cardinal (2011), Isotopic constraints on the Si-biogeochemical cycle of the Antarctic Zone in the Kerguelen area (KEOPS), *Mar. Chem.*, *123*(1–4), 11–22, doi:10.1016/j.marchem.2010.08.005.
Garreaud, R. D., M. Vuille, R. Compagnucci, and J. Marengo (2009), Present-day South American climate, *Palaeogeogr. Palaeoclimatol. Palaeoecol.*, *281*(3–4), 180–195, doi:10.1016/j.palaeo.2007.10.032.
Grasse, P., C. Ehlert, and M. Frank (2013), The influence of water mass mixing on the dissolved Si isotope composition in the Eastern Equatorial Pacific, *Earth Planet. Sci. Lett.*, *380*, 60–71, doi:10.1016/j.epsl.2013.07.033.
Grasse, P., E. Ryabenko, C. Ehlert, M. A. Altabet, and M. Frank (2016), Silicon and nitrogen cycling in the upwelling area off Peru: A dual isotope approach, *Limnol. Oceanogr.*, *61*, 1661–1676, doi:10.1002/lno.10324.
Gutiérrez, D., A. Sifeddine, D. B. Field, L. Ortlieb, G. Vargas Easton, F. P. Chávez, F. Velazco, V. Ferreira, P. Tapia, and R. Salvatteci (2009), Rapid reorganization in ocean biogeochemistry off Peru towards the end of the Little Ice Age, *Biogeosciences*, *6*, 835–848, doi:10.5194/bg-6-835-2009.
Hayes, C. T., R. F. Anderson, and M. Q. Fleisher (2011), Opal accumulation rates in the equatorial Pacific and mechanisms of deglaciation, *Paleoceanography*, *26*, PA1207, doi:10.1029/2010PA002008.
Hendry, K. R., and M. A. Brzezinski (2014), Using silicon isotopes to understand the role of the Southern Ocean in modern and ancient biogeochemistry and climate, *Quat. Sci. Rev.*, *89*, 13–26, doi:10.1016/j.quascirev.2014.01.019.
Hendry, K. R., R. B. Georg, R. E. M. Rickaby, L. F. Robinson, and A. N. Halliday (2010), Deep ocean nutrients during the Last Glacial Maximum deduced from sponge silicon isotopic compositions, *Earth Planet. Sci. Lett.*, *292*(3–4), 290–300, doi:10.1016/j.epsl.2010.02.005.
Huffman, G. J., R. F. Adler, D. T. Bolvin, and G. Gu (2009), Improving the global precipitation record: GPCP Version 2.1, *Geophys. Res. Lett.*, *36*, doi:10.1029/2009GL040000.
Huyer, A., R. L. Smith, and T. Paluszkiewicz (1987), Coastal upwelling off Peru during normal and El Niño times, 1981–1984, *J. Geophys. Res.*, *92*, 14,297–14,307, doi:10.1029/JC092iC13p14297.
Kessler, W. S. (2006), The circulation of the eastern tropical Pacific: A review, *Prog. Oceanogr.*, *69*(2–4), 181–217, doi:10.1016/j.pocean.2006.03.009.
Kienast, M., S. S. Kienast, S. E. Calvert, T. I. Eglinton, G. Mollenhauer, R. François, and A. C. Mix (2006), Eastern Pacific cooling and Atlantic overturning circulation during the last deglaciation, *Nature*, *443*(7113), 846–849, doi:10.1038/nature05222.
Kienast, S. S., M. Kienast, S. Jaccard, S. E. Calvert, and R. Francois (2006), Testing the silica leakage hypothesis with sedimentary opal records from the eastern equatorial Pacific over the last 150 kyrs, *Geophys. Res. Lett.*, *33*, L15607, doi:10.1029/2006GL026651.
Kienast, S. S., T. Friedrich, N. Dubois, P. S. Hill, A. Timmermann, A. C. Mix, and M. Kienast (2013), Near collapse of the meridional SST gradient in the eastern equatorial Pacific during Heinrich Stadial 1, *Paleoceanography*, *28*, 663–674, doi:10.1002/2013PA002499.
Koutavas, A., P. B. deMenocal, G. C. Olive, and J. Lynch-Stieglitz (2006), Mid-Holocene El Niño–Southern Oscillation (ENSO) attenuation revealed by individual foraminifera in eastern tropical Pacific sediments, *Geology*, *34*(12), 993, doi:10.1130/G22810A.1.
Krissek, L. A., K. F. Scheidegger, and L. D. Kulm (1980), Surface sediments of the Peru-Chile continental margin and the Nazca plate, *Geol. Soc. Am. Bull.*, *91*(6), 321, doi:10.1130/0016-7606(1980)91<321:SSOTPC>2.0.CO;2.
Levin, L. A. (2003), Oxygen minimum zone benthos: Adaptation and community response to hypoxia, in *Oceanography and Marine Biology: An Annual Review*, vol. 41, edited by R. N. Gibson and R. Atkinson, pp. 1–45, Aberdeen Univ. Press, London.

Loubere, P. (1999), A multiproxy reconstruction of biological productivity and oceanography in the eastern equatorial Pacific for the past 30,000 years, *Mar. Micropaleontol.*, *37*(2), 173–198, doi:10.1016/S0377-8398(99)00013-4.
MacIsaac, J. J., R. C. Dugdale, R. T. Barber, D. Blasco, and T. T. Packard (1985), Primary production cycle in an upwelling center, *Deep Sea Res., Part A*, *32*(5), 503–529, doi:10.1016/0198-0149(85)90042-1.
Makou, M. C., T. I. Eglinton, D. W. Oppo, and K. A. Hughen (2010), Postglacial changes in El Niño and La Niña behavior, *Geology*, *38*(1), 43–46, doi:10.1130/G30366.1.
Margalef, R. (1978), Life-forms of phytoplankton as survival alternatives in an unstable environment, *Oceanol. Acta*, *1*(4), 493–509.
McClymont, E. L., R. S. Ganeshram, L. E. Pichevin, H. M. Talbot, B. E. vanDongen, R. C. Thunell, A. M. Haywood, J. S. Singarayer, and P. J. Valdes (2012), Sea-surface temperature records of Termination 1 in the Gulf of California: Challenges for seasonal and interannual analogues of tropical Pacific climate change, *Paleoceanography*, *27*, PA2202, doi:10.1029/2011PA002226.
McGee, D., A. Donohoe, J. Marshall, and D. Ferreira (2014), Changes in ITCZ location and cross-equatorial heat transport at the Last Glacial Maximum, Heinrich Stadial 1, and the mid-Holocene, *Earth Planet. Sci. Lett.*, *390*, 69–79, doi:10.1016/j.epsl.2013.12.043.
Messié, M., and F. Chavez (2015), Seasonal regulation of primary production in eastern boundary upwelling systems, *Prog. Oceanogr.*, *134*, 1–18, doi:10.1016/j.pocean.2014.10.011.
Mohtadi, M. (2004), Mechanisms and variations of the paleoproductivity off northern Chile (24°S–33°S) during the last 40,000 years, *Paleoceanography*, *19*, PA2023, doi:10.1029/2004PA001003.
Mollier-Vogel, E. (2012), *Peruvian Oxygen Minimum Zone Dynamics During the Last 18 000 Years*, pp. 1–182, PhD thesis, Univ. of Kiel.
Mollier-Vogel, E., G. Leduc, T. Böschen, P. Martinez, and R. R. Schneider (2013), Rainfall response to orbital and millennial forcing in northern Peru over the last 18 ka, *Quat. Sci. Rev.*, *76*, 29–38, doi:10.1016/j.quascirev.2013.06.021.
Montes, I., F. Colas, X. Capet, and W. Schneider (2010), On the pathways of the equatorial subsurface currents in the eastern equatorial Pacific and their contributions to the Peru-Chile Undercurrent, *J. Geophys. Res.*, *115*, C09003, doi:10.1029/2009JC005710.
Montes, I., W. Schneider, F. Colas, B. Blanke, and V. Echevin (2011), Subsurface connections in the eastern tropical Pacific during La Niña 1999–2001 and El Niño 2002–2003, *J. Geophys. Res.*, *116*, C12022, doi:10.1029/2011JC007624.
Müller, P. J., and R. Schneider (1993), An automated leaching method for the determination of opal in sediments and particulate matter, *Deep Sea Res., Part I*, *40*(3), 425–444.
Nürnberg, D., T. Böschen, K. Doering, E. Mollier-Vogel, R. Schneider, and J. Raddatz (2015), Sea surface and subsurface circulation dynamics off equatorial Peru during the last ~17 kyrs, *Paleoceanography*, *30*, 984–999, doi:10.1002/2014PA002706.
Ochoa, N., and O. Gomez (1981), *Variaciones del Fitoplancton en el Área de Chimbote Durante 1977*, pp. 119–129, Boletin Instituto del Mar del Perú, Callao.
Ochoa, N., M. H. Taylor, S. Purca, and E. Ramos (2010), Intra- and interannual variability of nearshore phytoplankton biovolume and community changes in the northern Humboldt Current system, *J. Plankton Res.*, *32*(6), 843–855, doi:10.1093/plankt/fbq022.
Ortlieb, L., G. Vargas, and J.-F. Saliège (2011), Marine radiocarbon reservoir effect along the northern Chile–southern Peru coast (14–24°S) throughout the Holocene, *Quat. Res.*, *75*(1), 91–103, doi:10.1016/j.yqres.2010.07.018.
Pena, L. D., I. Cacho, P. Ferretti, and M. A. Hall (2008), El Niño-Southern Oscillation-like variability during glacial terminations and interlatitudinal teleconnections, *Paleoceanography*, *23*, PA3101, doi:10.1029/2008PA001620.
Pena, L. D., S. L. Goldstein, S. R. Hemming, K. M. Jones, E. Calvo, C. Pelejero, and I. Cacho (2013), Rapid changes in meridional advection of Southern Ocean intermediate waters to the tropical Pacific during the last 30 kyr, *Earth Planet. Sci. Lett.*, *368*(C), 20–32, doi:10.1016/j.epsl.2013.02.028.
Pennington, J. T., K. L. Mahoney, V. S. Kuwahara, D. D. Kolber, R. Calienes, and F. P. Chavez (2006), Primary production in the eastern tropical Pacific: A review, *Prog. Oceanogr.*, *69*(2–4), 285–317, doi:10.1016/j.pocean.2006.03.012.
Pichevin, L. E., B. C. Reynolds, R. S. Ganeshram, I. Cacho, L. Pena, K. Keefe, and R. M. Ellam (2009), Enhanced carbon pump inferred from relaxation of nutrient limitation in the glacial ocean, *Nature*, *459*(7250), 1114–1117, doi:10.1038/nature08101.
Pichevin, L. E., R. S. Ganeshram, W. Geibert, R. Thunell, and R. Hinton (2014), Silica burial enhanced by iron limitation in oceanic upwelling margins, *Nat. Geosci.*, doi:10.1038/ngeo2181.
Reimer, P. J., and E. Bard (2013), IntCal13 and Marine13 radiocarbon age calibration curves 0–50,000 years cal BP, *Radiocarbon*, *55*, 1869–1887.
Reimers, C. E., and E. Suess (1983), Spatial and temporal patterns of organic matter accumulation on the Peru continental margin, in *Coastal Upwelling Its Sedimentary Record Part B: Sedimentary Records of Ancient Coastal Upwelling*, *NATO Conf. Ser. IV: Mar. Sci.*, vol. 10B, edited by J. Thiede and E. Suess, pp. 311–346, Plenum Press, New York.
Rein, B. (2004), A major Holocene ENSO anomaly during the Medieval period, *Geophys. Res. Lett.*, *31*, L17211, doi:10.1029/2004GL020161.
Rein, B., A. Lückge, L. Reinhardt, F. Sirocko, A. Wolf, and W.-C. Dullo (2005), El Niño variability off Peru during the last 20,000 years, *Paleoceanography*, *20*, PA4003, doi:10.1029/2004PA001099.
Reinhardt, L., H. R. Kudrass, A. Luckge, M. Wiedicke, J. Wunderlich, and G. Wendt (2002), High-resolution sediment echosounding off Peru: Late Quaternary depositional sequences and sedimentary structures of a current-dominated shelf, *Mar. Geophys. Res.*, *23*(4), 335–351.
Reynolds, B. C., M. Frank, and A. N. Halliday (2006), Silicon isotope fractionation during nutrient utilization in the North Pacific, *Earth Planet. Sci. Lett.*, *244*(1), 431–443, doi:10.1016/j.epsl.2006.02.002.
Reynolds, B. C., et al. (2007), An inter-laboratory comparison of Si isotope reference materials, *J. Anal. At. Spectrom.*, *22*(5), 561, doi:10.1039/b616755a.
Reynolds, B. C., M. Frank, and A. N. Halliday (2008), Evidence for a major change in silicon cycling in the subarctic North Pacific at 2.73 Ma, *Paleoceanography*, *23*, PA4219, doi:10.1029/2007PA001563.
Robinson, R. S., M. A. Brzezinski, C. P. Beucher, M. G. S. Horn, and P. Bedsole (2014), The changing roles of iron and vertical mixing in regulating nitrogen and silicon cycling in the Southern Ocean over the last glacial cycle, *Paleoceanography*, *29*, 1179–1195, doi:10.1002/2014PA002686.
Rousseau, J., M. J. Ellwood, H. Bostock, and H. Neil (2016), Estimates of late Quaternary mode and intermediate water silicic acid concentration in the Pacific Southern Ocean, *Earth Planet. Sci. Lett.*, *439*(C), 101–108, doi:10.1016/j.epsl.2016.01.023.
Sachs, J. P., D. Sachse, R. H. Smittenberg, Z. Zhang, D. S. Battisti, and S. Golubic (2009), Southward movement of the Pacific Intertropical Convergence Zone AD 1400–1850, *Nat. Geosci.*, *2*(7), 519–525, doi:10.1038/ngeo554.
Salvatteci, R., et al. (2014a), Cross-stratigraphies from a seismically active mud lens off Peru indicate horizontal extensions of laminae, missing sequences, and a need for multiple cores for high resolution records, *Mar. Geol.*, doi:10.1016/j.margeo.2014.07.008.
Salvatteci, R., D. Gutiérrez, D. Field, A. Sifeddine, L. Ortlieb, I. Bouloubassi, M. Boussafir, H. Boucher, and F. Cetin (2014b), The response of the Peruvian upwelling ecosystem to centennial-scale global change during the last two millennia, *Clim. Past*, *10*(2), 715–731, doi:10.5194/cp-10-715-2014.

Sanchez, G., R. Calienes, and S. Zuta (2000), The 1997–98 El Niño and its effects on the coastal marine ecosystem off Peru, *Rep. Calif. Coop. Oceanic Fish. Invest.*, *41*, 62–86.
Schönfeld, J., W. Kuhnt, Z. Erdem, S. Flögel, N. Glock, M. Aquit, M. Frank, and A. Holbourn (2015), Records of past mid-depth ventilation: Cretaceous ocean anoxic event 2 vs. recent oxygen minimum zones, *Biogeosciences*, *12*(4), 1169–1189, doi:10.5194/bg-12-1169-2015-supplement.
Schrader, H. (1992), Comparison of Quaternary coastal upwelling proxies off central Peru, *Mar. Micropaleontol.*, *19*, 29–47.
Schrader, H., and R. Sorknes (1991), Peruvian coastal upwelling—Late Quaternary productivity changes revealed by diatoms, *Mar. Geol.*, *97*(3–4), 233–249.
Schuette, G. (1980), Recent marine diatom taphocoenoses off Peru and off southwest Africa: Reflection of coastal upwelling, PhD thesis, 125 pp., Oreg. State Univ.
Schuette, G., and H. Schrader (1981), Diatom taphocoenoses in the coastal upwelling area off South West Africa, *Mar. Micropaleontol.*, *6*(2), 131–155, doi:10.1016/0377-8398(81)90002-5.
Sifeddine, A., et al. (2008), Laminated sediments from the central Peruvian continental slope: A 500 year record of upwelling system productivity, terrestrial runoff and redox conditions, *Prog. Oceanogr.*, *79*(2–4), 190–197, doi:10.1016/j.pocean.2008.10.024.
Skillbeck, C. G., and D. Fink (2006), Data report: Radiocarbon dating and sedimentation rates for Holocene–Upper Pleistocene sediments, Eastern Equatorial Pacific and Peru continental margin, in *Proceedings of the Ocean Drilling Program Scientific Results*, vol. 201, pp. 1–15. [Available at http://www-odp.tamu.edu/ publications/201_SR/VOLUME/ CHAPTERS/108.PDF.]
Spero, H. J. (2002), The cause of carbon isotope minimum events on glacial terminations, *Science*, *296*(5567), 522–525, doi:10.1126/science.1069401.
Stott, L. (2002), Super ENSO and global climate oscillations at millennial time scales, *Science*, *297*(5579), 222–226, doi:10.1126/science.1071627.
Stramma, L., H. W. Bange, R. Czeschel, A. Lorenzo, and M. Frank (2013), On the role of mesoscale eddies for the biological productivity and biogeochemistry in the eastern tropical Pacific Ocean off Peru, *Biogeosci. Discuss.*, *10*(6), 9179–9211, doi:10.5194/bgd-10-9179-2013.
Strub, P. T., J. M. Mesias, V. Montecino, J. Rutllant, and S. Salinas (1998), Coastal ocean circulation off Western South America, in *The Sea*, vol. 11, edited by A. R. Robinson and K. H. Brink, pp. 273–313, John Wiley, New York.
Suess, E., L. D. Kulm, and J. S. Killingley (1987), Coastal upwelling and a history of organic-rich mudstone deposition off Peru, in *Marine Petroleum Source Rocks*, *Spec. Publ.*, edited by J. Brooks and A. J. Fleet, pp. 181–197, Geol. Soc. of London.
Sutton, J. N., D. E. Varela, M. A. Brzezinski, and C. P. Beucher (2013), Species-dependent silicon isotope fractionation by marine diatoms, *Geochim. Cosmochim. Acta*, *104*(C), 300–309, doi:10.1016/j.gca.2012.10.057.
Tarazona, J., D. Gutiérrez, C. Paredes, and A. Indacochea (2003), Overview and challenges of marine biodiversity research in Peru, *Gayana*, *67*(2), 206–231.
Timmermann, A., S. J. Lorenz, S.-I. An, A. Clement, and S.-P. Xie (2007), The effect of orbital forcing on the mean climate and variability of the tropical Pacific, *J. Clim.*, *20*(16), 4147–4159, doi:10.1175/JCLI4240.1.
Toggweiler, J. R., K. Dixon, and W. S. Broecker (1991), The Peru upwelling and the ventilation of the south Pacific thermocline, *J. Geophys. Res.*, *96*, 20,467–20,497, doi:10.1029/91JC02063.
Toggweiler, J. R., J. L. Russell, and S. R. Carson (2006), Midlatitude westerlies, atmospheric CO_2, and climate change during the ice ages, *Paleoceanography*, *21*, PA2005, doi:10.1029/2005PA001154.
Wyrtki, K. (1975), Fluctuations of the dynamic topography in the Pacific Ocean, *J. Phys. Oceanogr.*, *5*, 450–459.
Wyrtki, K. (1981), An estimate of equatorial upwelling in the Pacific, *J. Phys. Oceanogr.*, *11*(9), 1205–1214.
Xie, R. C., and F. Marcantonio (2012), Deglacial dust provenance changes in the Eastern Equatorial Pacific and implications for ITCZ movement, *Earth Planet. Sci. Lett.*, *317–318*, 386–395.
Zuta, S., and O. Guillén (1970), Oceanografía de las aguas costeras del Perú, *Bol. Inst. Mar. Perú*, *2*(5), 157–324.